Finite Element Analysis of

Micro-cantilever Beam Experiments in UO_2

by

Bowen Gong

A Thesis Presented in Partial Fulfillment
of the Requirements for the Degree
Master of Science

Approved November 2015 by the
Graduate Supervisory Committee:

Pedro Peralta, Chair
Jagannathan Rajagopalan
Kiran Solanki

ARIZONA STATE UNIVERSITY

December 2015

ABSTRACT

Uranium Dioxide (UO_2) is a significant nuclear fission fuel, which is widely used in nuclear reactors. Understanding the influence of microstructure on thermo-mechanical behavior of UO_2 is extremely important to predict its performance. In particular, evaluating mechanical properties, such as elasticity, plasticity and creep at sub-grain length scales is key to developing this understanding as well as building multi-scale models of fuel behavior with predicting capabilities. In this work, modeling techniques were developed to study effects of microstructure on Young's modulus, which was selected as a key representative property that affects overall mechanical behavior, using experimental data obtained from micro-cantilever bending testing as benchmarks. Beam theory was firstly introduced to calculate Young's modulus of UO_2 from the experimental data and then three-dimensional finite element models of the micro-cantilever beams were constructed to simulate bending tests in UO_2 at room temperature. The influence of the pore distribution was studied to explain the discrepancy between predicted values and experimental results. Results indicate that results of tests are significantly affected by porosity given that both pore size and spacing in the samples are of the order of the micro-beam dimensions. Microstructure reconstruction was conducted with images collected from three-dimensional serial sectioning using focused ion beam (FIB) and electron backscattering diffraction (EBSD) and pore clusters were placed at different locations along the length of the beam. Results indicate that the presence of pore clusters close to the substrate, i.e., the clamp of the micro-cantilever beam, has the strongest effect on load-deflection behavior, leading to a reduction of stiffness that is the largest for any location of the pore cluster. Furthermore, it was also found from both numerical and

analytical models that pore clusters located towards the middle of the span and close to the end of the beam only have a very small effect on the load-deflection behavior, and it is concluded that better estimates of Young's modulus can be obtained from micro-cantilever experiments by using microstructurally explicit models that account for porosity in about one half of the beam length close to the clamp. This, in turn, provides an avenue to simplify micro-scale experiments and their analysis.

DEDICATION

To my parents

ACKNOWLEDGMENTS

It is my honor to take this opportunity to thank professor Pedro Peralta, my advisor and mentor. I would not complete this thesis without his guidance and continuous support. It is him who always encourages me and pushes me forward. I appreciate his valuable suggestions and patient directions. I shall always remember the round table and whiteboard in his office where ideas occur. And I also appreciate professor Kiran Solanki and professor Jagannathan Rajagopalan for being my committee members.

I acknowledge all the journals, books and websites that are citied in this thesis. Such information provides me with detailed knowledge, methods and directions in this study.

I also wish to thank my colleague, Harn Chyi Lim, Robert Mcdonald, Benjamin Shaffer, and David Frazer. I can never finish my research work without their cooperation.

This work was performed with support from DOE/NE under grant # DE-NE0000670. The assistance of Darrin Byler, Erik Luther and Andrew Nelson at Los Alamos National Laboratory by providing UO_2 samples for this work is also greatly appreciated.

I think I should always be grateful to my parents. I miss them so much during the time I live and study overseas. I will stay close to them and accompany them when I have chance.

Special thanks must go to my roommates, Hechao Li for taking me fly and Shaohua Chen for his support and help. Many thanks to my friends: Juan Ji for being so supportive at the other side of the world, Tianyu Xi for offering me free meal plans sometimes when I am lazy to cook, Yifan Zhou for providing accommodation for such a

long time, Tianze Peng for being so helpful in many things, Feimi Yu for preparing for test together, Jinshan Lin for accompanying me in the gym, Hang Su for cooking so delicious noodles, and many other friends for our time learning and having fun together.

TABLE OF CONTENTS

Page

CHAPTER Page

CHAPTER Page

LIST OF TABLES

Table Page

LIST OF FIGURES

Figure Page

Figure Page

I INTRODUCTION

1.1 Nuclear Energy

1.1.1 History of Nuclear Energy

Since 1951, when the Experimental Breeder Reactor I (EBR-I) became the world's first nuclear power plant for electricity generating purposes, the nuclear energy industry in the US has experienced a high point, a stagnation period and a recent revival. One of the reasons nuclear energy is attractive is that with the consumption of fossil fuel such as petroleum and coal, the day is coming when there will be inadequate supplies of fossil fuels to maintain our current way of life. Given the ever-increasing demand for energy, nuclear power will become one of the best options for generating reliable electricity at a reasonable cost.

The stagnation of nuclear power came as a result from political and environmental concerns, which were amplified by well-known nuclear accidents, which occurred at Three Mile Island (United States, 1979) and Chernobyl (Ukraine, 1986). The public was in a panic about how damaging nuclear energy generation could be when they saw the negative influence of nuclear pollution. Several more problems, such as dealing with nuclear waste, transporting and storing nuclear materials, improving the reliability of radioactive materials and the proliferation problem, i.e., keeping nuclear-weapon grade materials produced in reactors safe, also contributed to the stagnation of the research on nuclear energy. Nowadays, with the problems of climate change and air pollution become more and more severe, developing nuclear energy has once again returned to the main stage and hopefully the safety of the nuclear energy will be enhanced and its reliability

will be largely improved this time. The recent accident in Fukushima (Japan, 2011), has led to renewed concerns, but not as pronounced as with the accidents mentioned above.

1.1.2 Development of Nuclear Power Plant

There are currently four mature generations in the development of nuclear reactors, and generation V has been theoretically proved, but not fully researched or implemented [1]. The roadmap of generations of nuclear power is shown in Figure 1.1 [1] and each of these reactors will be briefly discussed in this section.

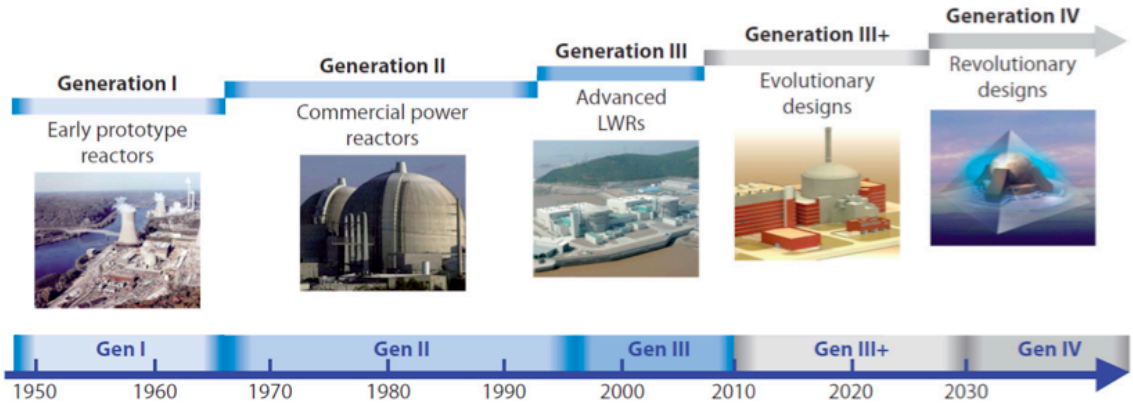

Figure 1.1: Generations of nuclear power: Time Ranges according to its design [1].

Generation I refers to the early prototypes, most of which were research reactors. The typical representatives of this generation are Shippingport in the United States, Uranium Naturel Graphite Gaz (UNGG) in France, and Dresden in the United States. These reactors were primarily experimental and the aim to build them was to verify nuclear technologies and to prove that nuclear power could be used to produce electricity.

Since late 1960s, generation II reactors were researched and greatly improved, with a typical lifetime of 40 years. Generation II reactors include pressurized water

reactors (PWR), Canada deuterium uranium reactors (CANDU), boiling water reactors (BWR), advanced gas-cooled reactors (AGR) and voda-vodyanoi energetichesky reactors (VVER) [1] and most of the current nuclear power plants belong to this generation.

Generation III is based on Generation II and improves fuel cycles to reduce nuclear waste, thermal efficiency to improve thermal exchange and safety to make it possible for a reactor to shut itself when a problem happens. In addition, reactors that belong to this generation have a longer lifespan, which is typically 60 years. Only four gen-III reactors are in operation today [1].

Generation IV was initiated in the 2000's and is currently being researched. This generation includes six types of reactors (Very-high-temperature reactor, Sodium-cooled fast reactor, Supercritical water reactor, Gas cooled fast reactor, Lead-alloy fast reactor, and Molten salt reactor) that bring technologies in all aspects to a new level and represent the future of nuclear energy. They have lower nuclear material cost, less material waste and safer designs. Nuclear power plants with generation IV reactors will possibly be constructed in the 2030s [1].

Although years of research and experience have enhanced the development of the nuclear power field, there are still many challenges for the nuclear power industry, which will be introduced in the next section.

1.1.3 Challenges of Nuclear Power

The challenges of nuclear power include costs, safety, nuclear waste and proliferation risks, as described below.

Costs

As reported in [2], the construction costs of nuclear plants are typically much higher than that of a coal or a natural gas plant, due to the long construction times and interest increase. The high initial costs make it hard for nuclear power to compete with coal and natural gas, although the costs for operation are lower than the other two and, what is more important, the price for nuclear energy is not subject to the volatility of oil prices. However, with the effort to lower the risk-premium and standardization of design, the cost of nuclear power (in 2009) could decrease from 8.4 ¢/kWh to 6.6 ¢/kWh, which could be competitive with coal (6.2 ¢/kWh) and natural gas (6.5 ¢/kWh) [2].

Safety

The safety issues in nuclear power always attract extensive attention, since some of the nuclear accidents in the past 40 years were destructive. However, these three accidents are the only major accidents that have occurred in nuclear industry history, which means that nuclear power is actually very safe, as compared to other means of generating electricity. In addition, given that the aim of design and operation of nuclear power plants is to minimize the possibility of accidents, the likelihood of a major accident happening in nuclear power plants is low and decreasing [2].

Nuclear Waste

Disposal of nuclear waste is a challenging task, since there is no mature technologies or systems to deal with this waste. Currently, nuclear waste, mainly spent nuclear fuel (SNF) is usually stored underwater in pools that are close to the power plants. Plans to store SNF deep underground do exist and can only be carried out in the Yucca Mountain repository or a viable alternative that is licensed by DOE or NRC [3]. When

the repository in Yucca Mountain (or elsewhere) is filled up, another repository will presumably be constructed and opened. The locations of SNF and high-level waste are shown in the map in Figure 1.2. Because nuclear waste contains almost 90 percent of Uranium, which can be still used as fuel for advanced fast reactors, most of the nuclear waste can actually be reused. Hence, another way to deal with nuclear waste is recycling, which both helps to make use of nuclear material more efficiently and accelerate the decay process for final waste to become a less harmful material [4]. Countries like France, Russia and Japan have a policy to reprocess the nuclear waste, while many other countries like the U.S. do not have polices to use spent fuel as a resource [4].

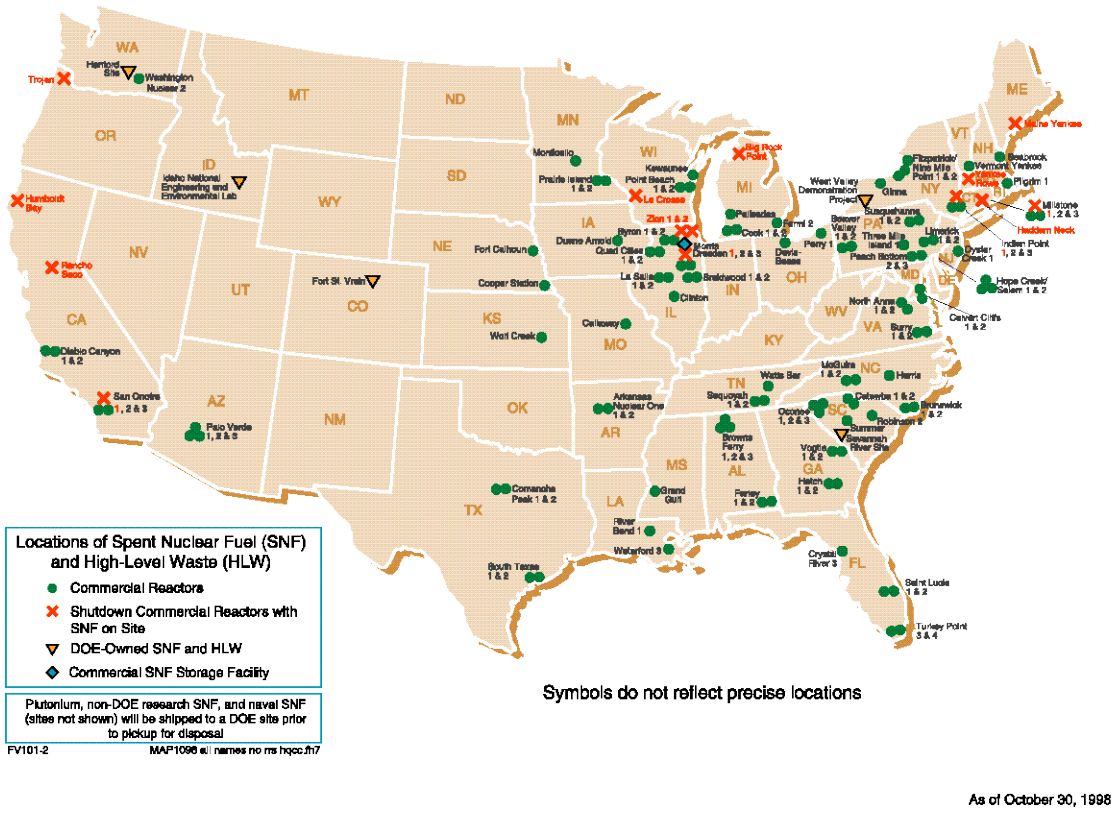

Figure 1.2: Nuclear Waste Locations in USA [5].

Proliferation Risks

Proliferation refers to the misuse of commercial nuclear facilities and operations to create nuclear weapons. To minimize and eliminate the spread of nuclear weapon technology, the International Atomic Energy Agency (IAEA) does inspect all the nuclear facilities all over the world to insure that nuclear material and technologies are only used for peaceful purposes, instead of building nuclear weapons [2].

1.1.4 Nuclear Energy Today

Since the establishment of the first experimental reactor in 1951, nuclear energy was introduced to produce electricity. In the following years, the cheap and emission-free electricity impressed the governments of many countries and nuclear energy has become an indispensable source for electricity all over the world. In 2015, there are more than 400 commercial nuclear power reactors in 31 countries [6] and they contribute to more than 10% of the world's electricity [7], as shown in Figure 1.3.

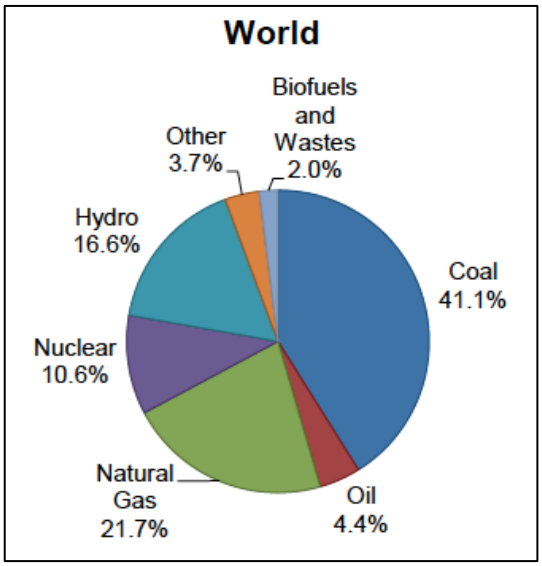

Figure 1.3: Share of different source of electricity generation worldwide [7].

The share of nuclear energy in electricity production of different countries can be seen in Figure 1.4 and it can be noticed that France has the highest share: nuclear power is its main source of electricity production. United States, Canada, Russia and some of the other European countries also rely on nuclear power as an important energy source. In the future, although there seems to be many challenges for nuclear power, the nuclear energy option is very likely to be retained and developed, with the efficiency of nuclear power generation being increased while the costs of it lowered. It is also believed that the safety standards will be improved and the challenges in the management of radioactive wastes will be ameliorated [2].

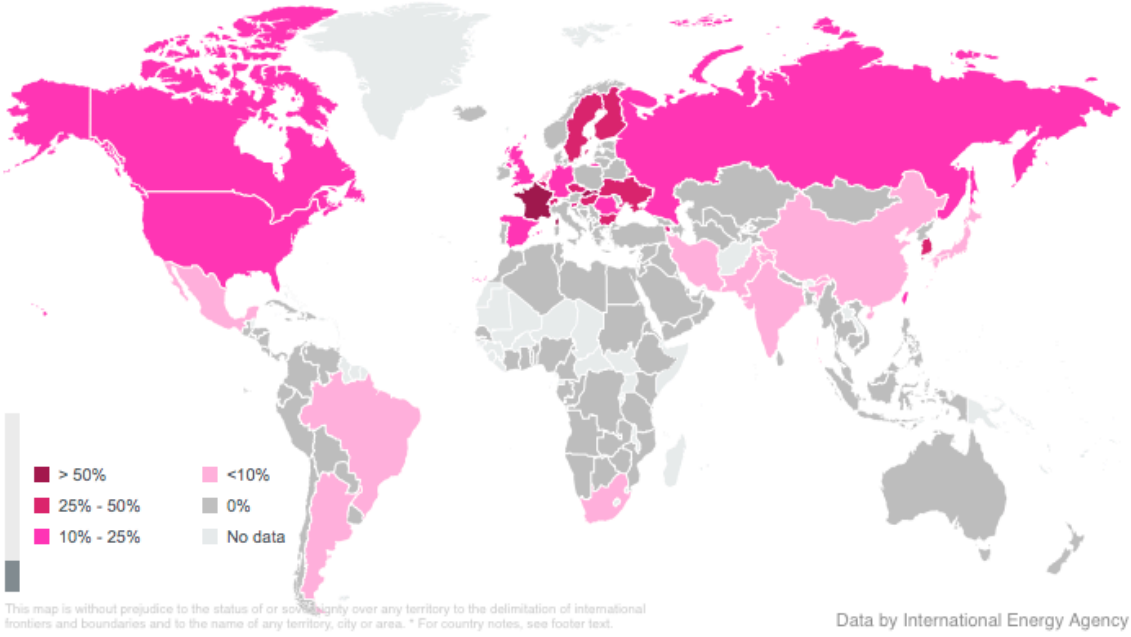

Figure 1.4: Share of nuclear in electricity production of the world [8].

Nuclear fuels are the most important part in the nuclear power industry. Its fabrication and the problems they have, as well as the motivations to create advanced accident-tolerant fuels will be introduced in the following sections.

1.1.5 Nuclear Fuels

Uranium dioxide is often used as the fuel for power plants and the process to make fuel from uranium involves several steps: mining, conversion, enrichment and fabrication. There are many techniques that can be used to get uranium, including surface mining, underground mining and in situ leaching. In situ leaching, also known as in situ recovery, is currently the most common technique to obtain uranium. About 47% of the world's uranium was mined using this technique [9]. After filtering and drying, uranium

becomes a uranium oxide concentrate. Then comes the step of enrichment, which is required by most nuclear power reactors. In the enrichment process, uranium oxide is first converted to uranium hexafluoride, which is a gas, to enable the fuel to be enriched. Then the proportion of ^{235}U is enriched from natural level of 0.7% to 3 to 5%. When fabricating fuel, enriched uranium hexafluoride is converted to uranium dioxide powder and then pressed into fuel pellets [10]. After that, fuel pellets are loaded into metallic tubes, typically made of zirconium or iron-nickel-chromium alloys, to form a fuel rod. The last step is to gather fuel rods together to form a fuel assembly, as shown in Figure 1.5.

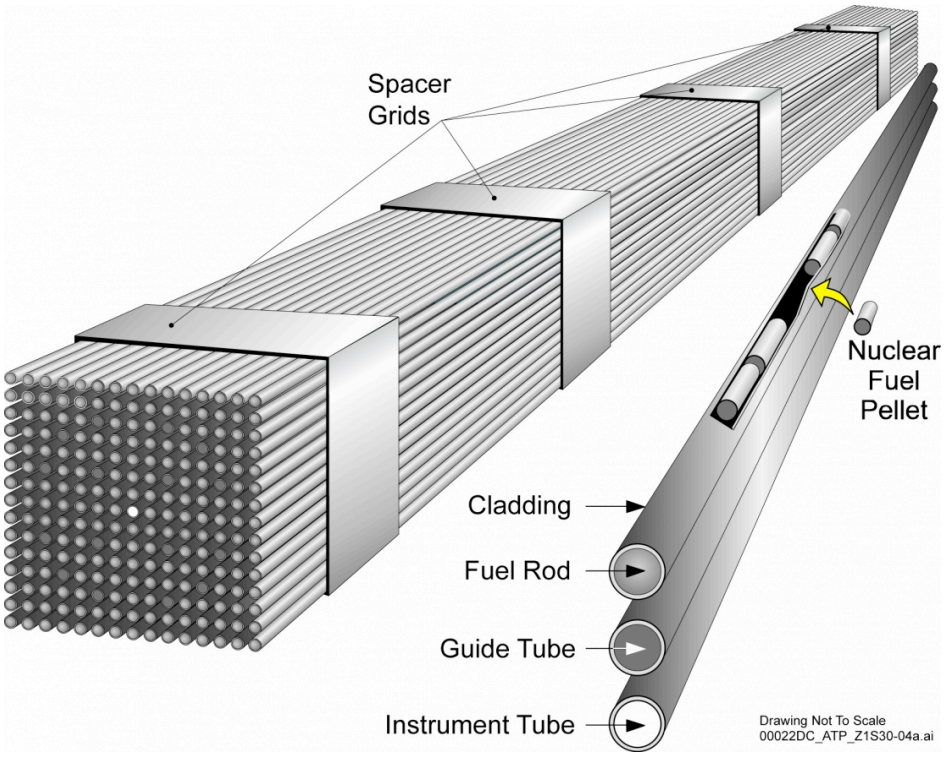

Figure 1.5: Fuel assembly containing nuclear fuel rods that are filled with fuel pellets [11].

The main process for fuels to generate energy is nuclear fission, which will be introduced in the next section.

1.1.6 Nuclear Fission

Nuclear fission of heavy elements was first discovered in 1938 and it is a nuclear reaction where the nucleus of an atom, such as ^{235}U, absorbs a neutron, becomes instable and splits into lighter elements. The process will release a huge amount of energy, which can be utilized to generate electricity. When nuclear fission happens, more neutrons will be released during the process, and these neutrons can be absorbed by the nuclei of other atoms and the process repeats. The number of neutrons doubles each generation, so does the number of fissions. In the nuclear fission process, the nuclei can break into any combination of lighter nuclei and normally it is not likely for them to break into two equal nuclei, but slightly unequal [12].

1.1.7 Fuel Swelling

Since nuclear fission will be most likely to break one atom into two, the number of atoms will increase dramatically as fission progresses. If we assume that every atom holds about the same volume, the volume of the nuclear fission product will increase. Although some of the products depart from the fuel and compensate for the volume increase, some of the gaseous fission products will be retained by fuel and balance the departed part. The net result is a fractional increase in the volume of the solid fuel of about 0.8 times the burnup, which is a measure of energy extracted from a primary nuclear fuel source [13]. Figure 1.6 shows a fuel pellet after swelling.

Figure 1.6: Effect of fuel swelling [13].

1.1.8 Loss of Coolant Accident (LOCA) and Pellet-cladding Mechanical Interaction (PCMI)

Loss of coolant accident (LOCA) is a failure mode happens in a nuclear reactor when coolant is scarce in the reactor circuit [14]. When abnormal activity, such as the reduction of coolant flow, is detected by the control system, the emergency core cooling system (ECCS) will come into work and stop the fission chain reaction immediately. Although the reactor is scrammed and the power generated is reduced greatly, the level of decay heat will increase and result in the release of a great amount of heat, which can account for 7% of the thermal rating of the reactor [15] and lead to a steep temperature increase. When temperature increases, thermal stresses that exceed the fracture stress of UO_2 will be generated in the fuel pellet as a consequence of the radial temperature gradients and will turn the pellet into an hourglass shape, as shown in Figure 1.7a. The hourglass shape happens because of the switch from plane-strain conditions near the pellet mid-plane to plane-stress condition at the upper and lower faces [16].

Although the thermal expansion coefficient of the cladding tube is typically large, as the temperature increases the gap is reduced. It happens some times that the pellets and cladding come into contact and interact with each other mechanically. When fuel pellets touch the cladding tube, the temperature of the cladding will rise drastically, leading to its eventual deformation to take the shape of the pellet, as shown in Figure 1.7c.

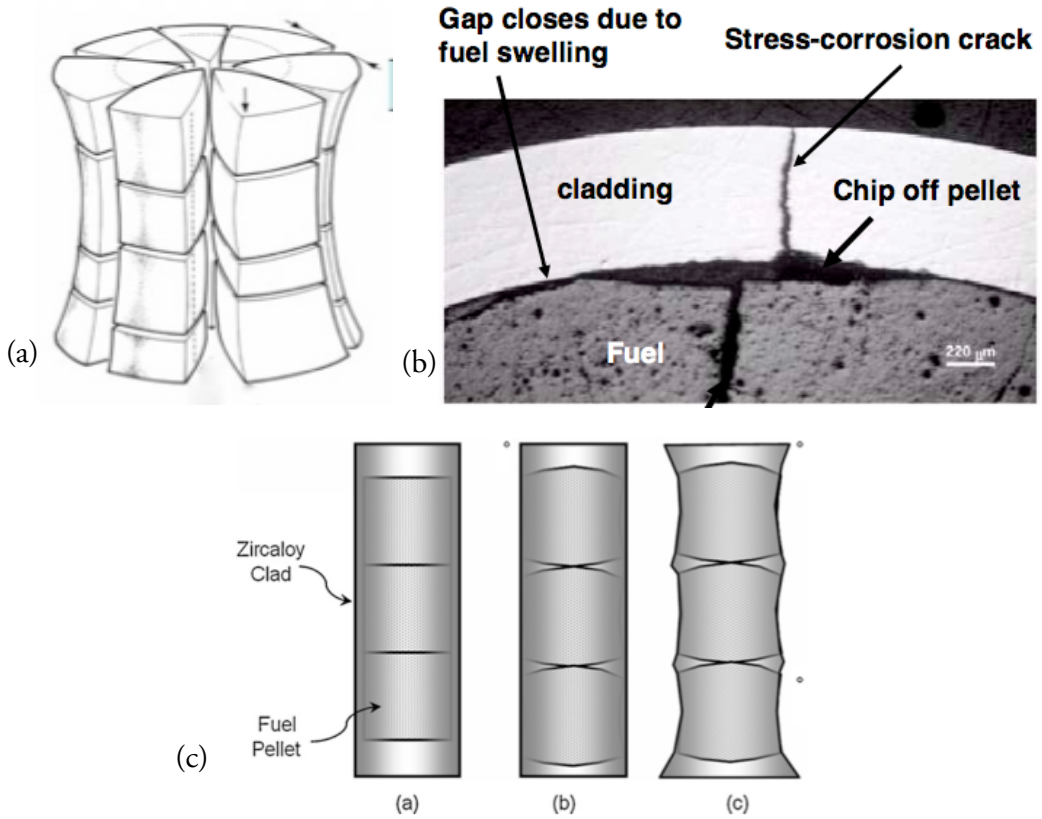

Figure 1.7: (a) Hourglass shape of UO_2 pellet in the fuel swelling [16]; (b) Consequence of PCMI; (c) The cladding tube deforms and takes the shape of pellets.

Stress in tension will be generated in the cladding axially and radially and leads to cladding failure. This phenomenon is called pellet-cladding mechanical interaction

(PCMI), which is one of the consequences of reactivity-initiated accidents (RIA). After the fuel pellets touch the cladding tube, the temperature of the tube will increase further and approximately reach 1000 K, which, according to Cacuci [17], will cause decrease of stiffness in the cladding tube and eventually contribute to its rupture. In the next stage, when the abnormal activity is detected, the emergency core cooling system will be activated [14] and contribute to the quenching of the surface of the cladding tube, which will ultimately result in crack formation.

Due to the problems such as swelling and PCMI, it is important to create new fuels that have better performance at normal and higher temperature, to mitigate the negative effects of these problems.

1.1.9 Advanced Accident-Tolerant Fuels

In order to improve the economic operations of nuclear power plants while ensuring safety, nuclear fuels and claddings with enhanced accident tolerance are being developed [18]. These fuels can tolerate loss of active cooling in the reactor core for a considerably longer time while maintaining or improving the fuel performance during normal operations [18]. Also, for the purpose of mitigating the consequences of fuel failure when temperature increases, the new fuel should possess the following features:

Slower Hydrogen Generation Rate: Hydrogen is generated in the reactor vessel because of the rapid oxidation of cladding and can hardly be avoided. Under a high temperature steam environment, the generation of hydrogen can lead to energetic explosions. Besides, the diffusion of the hydrogen into the unoxidized part of the cladding tube can lead to embrittlement of the cladding and eventually cause cladding

failure [18]. A cladding material with the capability to resist oxidation is desired, which will help to reduce hydrogen gas generation rate.

Greater retention of Fission Products: Both solid and gaseous fission products can be released to the environment when cladding fails. At this time, the retention of fission products into the fuel is quite important. Although it is very hard for the fuel to retain all of the fission products, it can be considered a great advancement if part of these products can be retained into the fuel [18].

Improved Cladding Reaction with Steam: The exposure of fuel pellets and cladding to high temperature steam can intensify oxidation reactions and lead to hydrogen generation. Hence, cladding tube materials with both the ability to resist oxidation under high temperature steam and higher mechanical strength is required.

Improved Fuel-Cladding Interactions: Since the behavior of the fuel is significant in the event of cladding failure, its properties under room temperature and high temperature are of great interests and need to be understood. Fuels with reduced chemical and mechanical interactions with the cladding, higher melting point, and lower operating temperature are preferred and desired [18].

Nowadays, the standard fuel-cladding system for commercial light water reactions (LWR) in the U.S. is Uranium dioxide and Zirconium-alloy (UO_2-Zr) [18]. In order to design and develop advanced fuels and claddings with improved accident tolerance that satisfy the features stated above, it is extremely important to understand the behavior and evaluate the performance of the fuels and claddings being employed currently under different environments.

During the past forty years, a large amount of basic and applied research has been conducted to support the performance of LWR fuel and claddings during normal power operations and accident conditions [18]. In this research work, different materials for cladding tubes were studied. From the stainless steel in the 1940s to zirconium alloys in the 2000s, till OPT ZIRLO and X5A [14] that are being developed, many constituents like tin, iron, chromium, nickel, and niobium have been added to the initial materials for better operation in water cooled reactors. Many mechanisms, such as creep and corrosion were also studied. These two failure modes happen together until the cladding tube breaks. In Zirconium alloys, when creep happens, deformation at 600 °C to 700 °C will cause dynamic recrystallization. When temperature reaches 820 °C to 980 °C, a phase change from α to β will happen and affects creep strength and fracture strain [19].

On the other side of the picture, the research of the fuel is also important. New fuels with enhanced accident tolerance have the capability to tolerate LOCA for a much longer period of time and at much higher temperature while improving fuel performance parameters, such as improved thermo-mechanical properties, fission product retention and lower operating temperatures [18]. As stated above, to create new fuels with better features, it is vital to study and understand the performance of the fuels being used currently, i.e., the properties of UO_2. Among all of the properties, the thermo-mechanical properties of the fuel are among the most important for overall fuel performance. Thus, careful experimental measurements of thermo-mechanical properties are key for the validation of robust fuel performance codes.

In UO_2, the thermo-mechanical response at the meso-scale depends strongly on crystallography of individual grains; therefore, a thorough study of the mechanical

response at the sub-grain level will be key to validate advanced fuel performance codes with multi-scale predictive capabilities [20]. In that regard, it makes sense to conduct experiments in single crystals. However, it can be complicated and expensive to prepare and produce macroscopic mono-crystalline samples, particularly after irradiation. In contrast, micro-scale mechanical testing provides the means to measure material properties at the sub-grain scale to study elastic and plastic behavior inside individual grains and there is no need to make mono-crystalline samples. Another benefit is that when testing at the micro-scale level, radiation doses of samples can be kept to a comparatively low level [19].

1.2 Micro-scale properties of UO_2

1.2.1 Elastic Anisotropy of UO_2

Since elastic properties are among the most basic properties of any material, it is quite reasonable that the research work starts with the study of elastic properties of UO_2. It is well known that UO_2 is anisotropic, which means that the physical and mechanical properties differ with orientation. If the anisotropic elastic stiffness can be obtained accurately, the same technique can also be used for further studies, such as plastic anisotropy. The mechanism for anisotropy is that atoms can slip over one another or distort in relation to one another easier in some directions than others [22]. In that regard, Young's modulus of mono-crystalline UO_2 is a function of crystal orientation and can be obtained using the equation deduced in [23] (shown below in Eq. 1) and the anisotropic elastic constants reported in [24]. The equation connects the reciprocal of Young's

modulus in the direction of the unit vector $\mathbf{l}_i$ with elastic compliance constants s_{ij}, which, for a cubic structure, such as uranium dioxide, results in the following relationship:

$$\frac{1}{E} = s_{11} - 2\left(s_{11} - s_{12} - \frac{1}{2}s_{44}\right)(l_1^2 l_2^2 + l_2^2 l_3^2 + l_3^2 l_1^2) \quad (1)$$

Elastic constants at high temperature of uranium dioxide are listed in Table 1.1, as reported by Fritz in 1976 [24]. Using these values and the procedure described in [23], a parametric surface of uranium dioxide showing values of Young's modulus along different orientations can be plotted, as shown in Figure 1.8.

Table 1.1: Elastic constant of UO_2 [24].

Elastic Constant (10^{12} dyn/cm^2)	Value
C_{11}	3.893
C_{12}	1.187
C_{44}	0.597

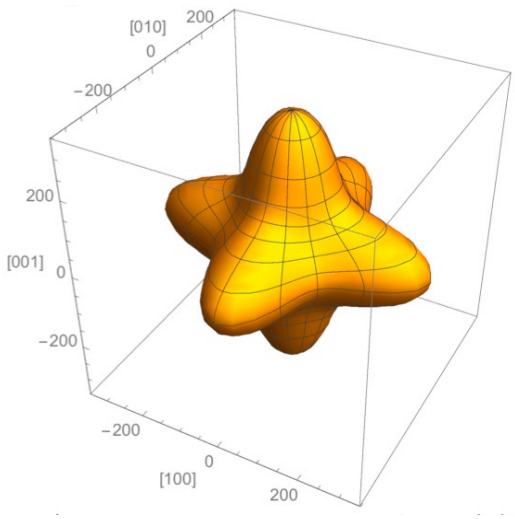

Figure 1.8: Variation of Young's modulus with orientation for UO_2.

It is expected that materials with a high degree of elastic anisotropy may show the most extreme elastic behavior and the Zener ratio Z, defined in Eq. 2, can be used as a measure of anisotropy of elastic behavior for cubic single crystals [25].

$$Z = \frac{2C_{44}}{C_{11} - C_{12}} \tag{2}$$

For uranium dioxide, Z equals 0.441, which is smaller than unity. This agrees with the fact that the maximum value of Young's modulus is along <100> and the minimum is along <111>. A simple calculation shows that the maximum possible value equals 333.8 GPa, which is obtained along <100>, and the minimum possible value equals 163.5 GPa, which is obtained along <111>. Since the ratio of maximum and minimum value of Young's modulus is 2.04, uranium dioxide has a moderate elastic anisotropy.

Techniques are needed for the purpose of measuring relevant properties at sub-grain scales using depleted uranium dioxide samples with different grain size and crystallography, which can be characterized using scanning electron microscopy and electron backscattering diffraction. Grains need to be carefully selected based on their crystallographic orientations to perform micromechanical testing using samples machined via focused ion beam.

Two options are available for micromechanical experiments, one is micro-cantilever bending (Figure 1.9 (a)) and another one is micro-pillar compression (Figure 1.9 (b)). Micro-pillar compression has been widely used for several years. Focused ion

beam is used to create a cylindrical sample with uniform cross section and one end of the sample is attached to the bulk substrate [26]. Then a nanoindentation setup is used to compress (or pull) the pillar and a stress-strain curve can be obtained. The advantages of this method are that the micro-pillar diameter can be flexible from 100 um to 100 nm, the micro-pillar can be manufactured on various materials, and many properties, such as Young's modulus, yield strength, and fracture strength can be obtained from the test. However, the load applied to the micro-pillar should be uniaxial, or the micro-pillar might distort and make the measurement inaccurate. Young's moduli values measured directly from compression tests tend to significantly underestimate the elastic modulus and they need to be corrected for the compliance of the substrate [27].

(a) 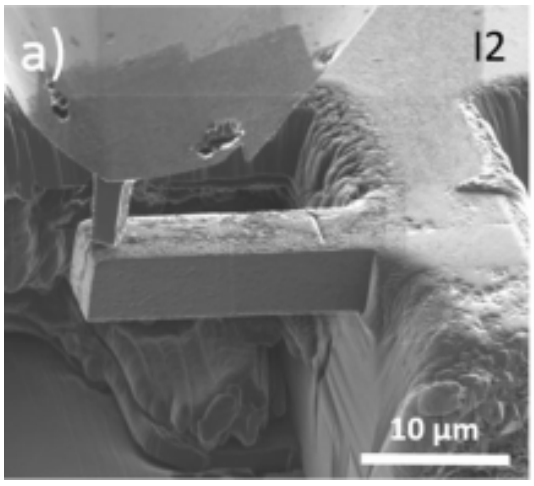

(b) 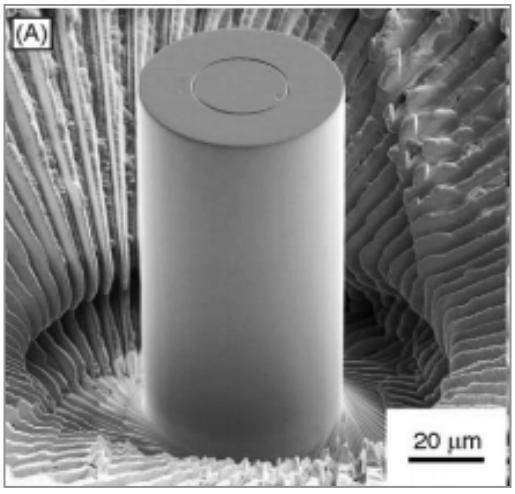

Figure 1.9: (a) Micro-Cantilever bending test [28]; (b) Micro-pillar compression test [29].

Another option is micro-cantilever bending. In comparison to micro-pillar compression, it has several advantages: Micro-cantilever beam is easier to fabricate than micro-pillar and it has much less problems with alignment. It is also relatively easy to

analyze to obtain elastic modulus and yield strength using micro-cantilever bending test. Besides, Armstrong et al. [30] have shown that this technique can accurately reflect Young's modulus of copper and can facilitate testing along particular crystal orientations. Based on the advantages of micro-cantilever technique, it was selected to conduct microstructural experiments of uranium dioxide.

1.2.2 Geometry of the Cantilever Beam

Two geometries are typically used for fabrication and testing of micro-cantilever beams. The first geometry is a rectangular parallelepiped (Figure 1.10 (a)), which is simple and easy to fabricate. The advantage for this geometry is that it is easy to analyze and the disadvantage is that it can only be placed along the sample's edge, which greatly limits the location to conduct micromechanical tests. The second geometry (Figure 1.10(b)) proposed by Maio and Roberts in 2004 [31] has a pentagonal cross section. This geometry is harder to manufacture but has the advantage that it can be placed anywhere on the sample surface. The Maio and Roberts geometry was eventually chosen for this work due to this advantage.

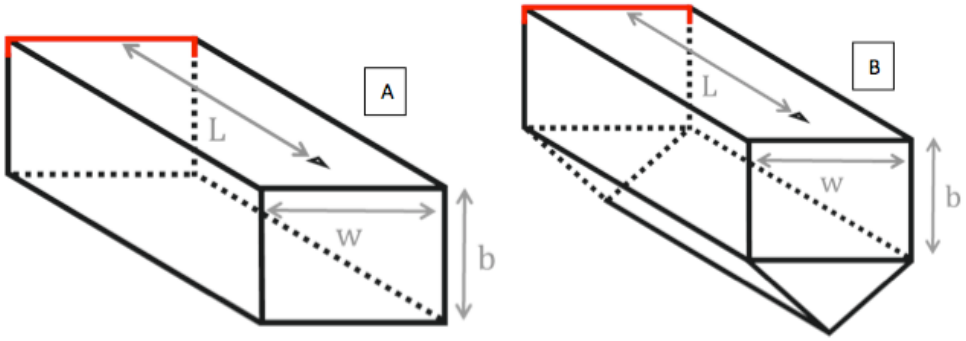

Figure 1.10: Two options for the geometry of the beam, (a) Rectangular parallelepiped; (b) The geometry proposed by Maio and Roberts [31].

1.2.3 Beam Theory

Simple beam theory can be used to calculate Young's modulus of uranium dioxide using experimental data from bending tests. Beam theory shows that there is a relationship between compliance, Young's modulus, moment of Inertia of the cross section, and the length of the beam, as reflected by Equations 3 through 4 [31]:

$$S = \frac{\delta}{P} = \frac{3}{3EI} \tag{3}$$

$$I = \frac{wb^3}{12} + (y - \frac{b}{2})^2 bw + \frac{w^4}{288} + [\frac{w}{6} + (b - y)]^2 \frac{w^2}{4} \tag{4}$$

$$y = \frac{\frac{b^2 w}{2} + \frac{w^2}{4}(b + \frac{w}{6})}{bw + \frac{w^2}{4}} \tag{5}$$

Where S is compliance and is obtained from load-displacement curve, P is the load applied, δ is displacement corresponding to the load point, E is Young's modulus, I is moment of inertia, y is vertical distance between neutral plane and upper surface [31] and L is the length of the beam. In the equation for I and y, b is width of the beam, w is the height of the rectangular parallelepiped part of the beam, which can be seen in Figure 1.11. The requirement for beam theory to work is that length to height ratio should be greater than 6, because the micro-cantilever beam is not fully fixed at the substrate [30]. The flexible substrate will introduce additional flexibility, which will introduce errors when measuring displacement at load point.

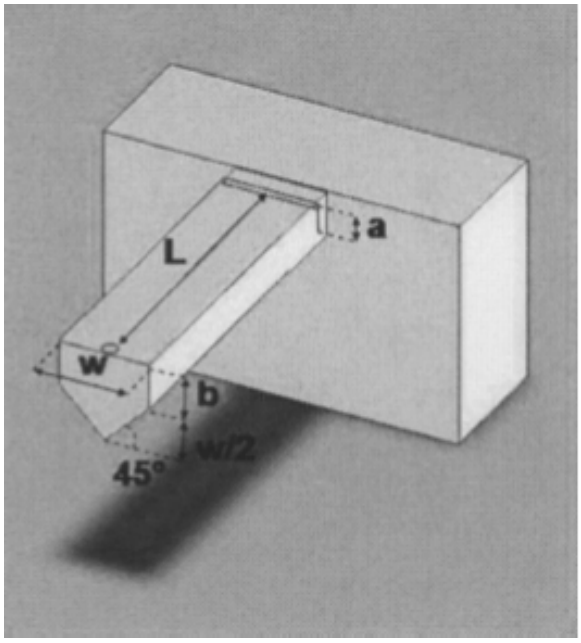

Figure 1.11: Dimension of the beam [31].

1.3 Effect of Porosities in Mechanical Properties of UO_2

Porosity is found to be significant for the performance of oxide nuclear fuels and has a very important influence on the mechanical properties, such as Young's modulus of UO_2 [32]. Hence, when experimental and modeling works are being carried out, it is very important to consider the influence of pores on the behavior of UO_2. Due to the fact that the size and spacing of the pores are comparable to the expected dimensions of the micro-cantilever beams, which means that the effects of porosity cannot be homogenized as is the case for large specimens [33], i.e., when the volume of the sample is large enough to be a Representative Volume Element (RVE). When the sample is smaller than RVE, elastic moduli can differ significantly from average values [33], and this must be taken account for the correct interpretation of experimental results obtained from micro-scale testing in porous materials.,

Note that even for large polycrystalline samples, the presence of porosity can affect the elastic properties of UO2 significantly, given that an exponential relationship was predicted between Young's modulus and porosity [34]. The relationship gives:

$$E = 2.196\times10^{12}e^{-3.025P}\ dynes/cm^2 \tag{6}$$

Where P is porosity. Due to the exponential relationship between porosity and Young's modulus, Young's modulus decreases rapidly when porosity increases. The plot below shows clearly their exponential relationship.

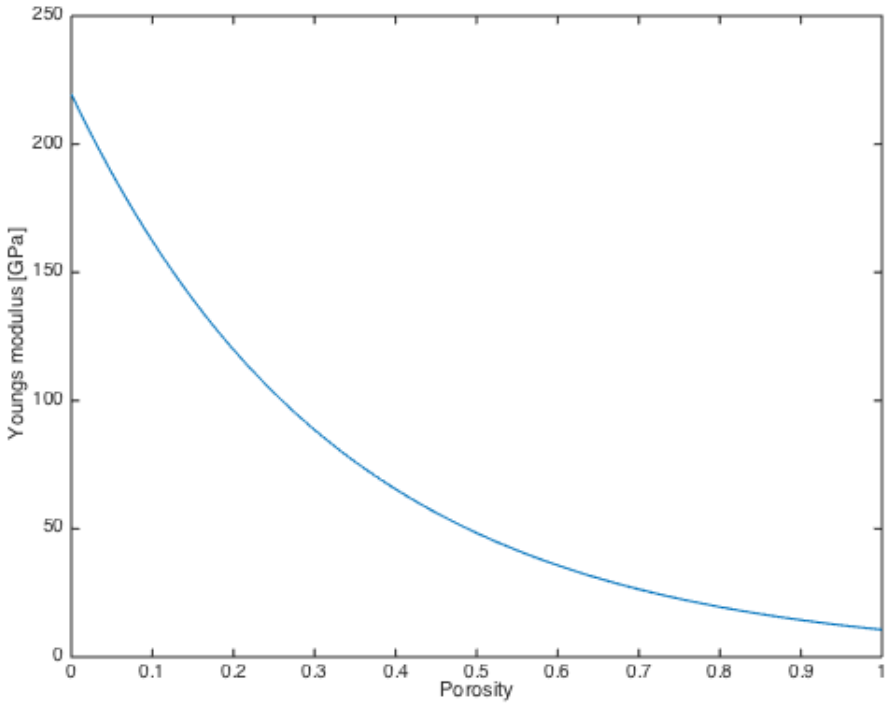

Figure 1.12: The relationship between Young's modulus and porosity, plotted according to equation (6).

Although this equation works quite well with bulk material, when the sample is smaller than the RVE, the shape of pores and the location of them can make it much harder to calculate the actual Young's modulus. Many experimental and modeling works have been carried out to study the impact of porosity on mechanical properties. Atomistic simulation models were generated [35] to describe the influence of porosity on the mechanical and thermal properties of UO_2 matrix; voids with different size, orientation and shape were studied, as well as their evolution [36]; effective elastic moduli were derived as a function of matrix properties, porosity and pore shape [37]; the finite element method has been used to study the influence of porosity and pore shape on the

elastic properties of model porous ceramics [37]. However, the pores in these models are all randomly distributed and cannot reflect the actual condition faced in our experiments; thus, these methods cannot be used to study the effect of the location of pores on elastic moduli of micro-cantilever beams described in this work. In this work, microstructure reconstruction, which can accurately reflect the size and location of pores, must be performed using images collected from 3-D serial sectioning and EBSD. Hence, the location and size of each pore can be reflected directly from the model created and the effects of these two parameters can be studied. Given how porosity can affect the properties, it is important to have a clear idea of the baseline value of these properties to perform effect comparisons. These baseline properties are discussed in the next section.

1.4 General and Mechanical Properties of UO_2

Uranium is a slivery-white metal that is weakly radioactive. Uranium is found as U-238, U-235 and U-234 (very small amount) in nature and is widely used as fuel for nuclear power plants. The energy that Uranium can produce is tremendous: one kilogram of U-235 can produce about $2*10^{13}$ joules of energy [38].

Uranium Dioxide is an oxidative product of uranium and is also used as fuel for nuclear fuel. To produce pure uranium dioxide, hydrogen is used to reduce uranium trioxide. The general properties of UO_2 are listed in table 1.2 and some of the reported mechanical properties of UO_2 are listed in table 1.3.

Table 1.2: General properties of Uranium Dioxide.

Name	Uranium Dioxide
Symbol	UO_2
Appearance	Black powder
Density	10.97 g/cm^3
Molar mass	270.03 g/mol
Melting point	3138 K
Crystal structure	Cubic

Table 1.3: Mechanical properties of Uranium Dioxide [39].

Young's modulus	2.19 x 10^8 kN/m^2
Shear modulus	8.14 x 10^8 kN/m^2
Poisson's ratio	0.345
Elastic constant	C_{11} = 3.893e11
Elastic constant (Cont'd)	C_{12} = 1.187e11
Elastic constant (Cont'd)	C_{44} = 0.597e11

II OBJECTIVES

In Chapter I, the significance of UO_2 as a fuel and the issues faced in the nuclear power industry were described. In order to create advanced accident-tolerant fuels that will benefit the current fleet and the next generation of commercial nuclear power reactors and provide a safe and reliable operation, it is necessary to understand the performance of the current fuel system. A significant amount of work has been carried out on the properties and behavior of UO_2 in nuclear reactors; however, most of them are devoted to the macro-scale properties; studies of performance of UO_2 at the sub-grain level are scarce. However, these properties can be significant in explaining its thermo-mechanical response at the meso-scale. Due to the fact that elasticity is one of the most fundamental properties of any material, it was considered reasonable to start this research work with the study of elastic properties of UO_2.

In that regard, the objective of this research is to create and develop simulation tools to study mechanical properties, in particular, elastic moduli of uranium dioxide at the sub-grain scale. Modeling will be implemented using finite element methods with both isotropic and anisotropic elastic properties that account for the effects of crystal anisotropy, stress, and porosity. Experimental work, i.e., microstructural bending tests at room temperature will be performed simultaneously by Peter Hosemann and David Frazer, our collaborators at the University of California, Berkeley (UCB) to validate the micro-scale results and study potential size effects. Four key objectives need to be accomplished

(a) Grain growth in UO_2 samples

Samples of Uranium dioxide need to be heat treated for a period of time to allow single crystal grains grow to a certain size that can facilitate the manufacturing process of micro-cantilever beams described in the next step. The heat treatment was carried out by ASU collaborators,

(b) Micro-cantilever fabrication and bending tests

Micro-cantilever beams need to be fabricated in selected grains with orientations of interest using focused ion beam (FIB) and then micromechanical bending tests must be carried out to obtain load-displacement data. The fabrication of these beams and their testing was carried out at UCB.

(c) Initial Data analysis

Data obtained in the micro-bending tests need to be used to calculate Young's modulus, accompanied with the beam theory and compared to existing data for UO_2 with and without porosity correction to evaluate discrepancies between measured values that might originate from anisotropy and the presence of porosity.

(d) Modeling and simulation

Models with the same geometry as the experiments need to be created and the same load must be applied to the same location on the beam, for the purpose of evaluating the experimental results. Models with pores are of particular interests in this work, since it is found that the size and spacing of pores are of the magnitude comparable to the dimension of the micro-cantilever beams. The effect of the location of the pores on Young's modulus needs to be studied to find appropriate modeling techniques to extract mechanical properties of the UO_2 matrix at the sub-grain scale from micro-scale experiments. This is the most important objective of this work.

III EXPERIMENTAL AND MODELING PROCEDURE

To achieve the goal of understanding micro-scale mechanical properties of uranium dioxide, the overall project that serves as an umbrella to this work combines experimental and modeling methods. The former provides the foundation for the modeling methodology used here, and, therefore, will be briefly described to provide a complete picture of this foundation and to motivate the choices made during the model formulation and analysis.

In the experimental procedure, samples were heat-treated by co-workers H. Lim, R. McDonald and B. Shaffer at ASU first to grow the grains to larger size and then micro-cantilever beams were manufactured at UCB such that they contained a single grain or a few grains. Micro-cantilever bending tests were then performed, also at UCB, to obtain load-deflection data and beam theory was used to calculate Young's modulus. These experimental results showed the need to formulate numerical models of the beams, to account for effects of beam geometry, compliance of the substrate, elastic anisotropy, and influence of pore size and location, among other. Therefore, models with the same geometry and dimensions as the actual beams used in the experiments were created in Abaqus™ to simulate the bending process and account for the effects mentioned above, where HyperMesh™ was used to delete selected elements from the beam for the purpose of studying simulated pore effects in UO_2.

In addition, microstructure reconstruction performed via Avizo™ was performed with images collected from 3-D serial sectioning using Focused Ion Beam (FIB) and Electron backscatter diffraction (EBSD) to study the effect of actual porosity on Young's modulus. Details on these procedures will be provided in this chapter.

3.1 Experimental procedures

3.1.1 Heat Treatment of d-UO_2 to Increase Grain Size

To accomplish the goal of performing and analyzing bending tests of micro-cantilever beams in d-UO_2 to study its sub-grain level behavior, samples with large grain size are needed. Given that the UO_2 fuel pellets typically have grain sizes ranging from 5 to 10 μm [39], it is extremely important to develop heat treatments to produce samples with larger grains. It has been shown that grains grow very fast in uranium dioxide when heat-treated in air at high temperatures [40]; however, the temperature required is higher than what available furnaces could reach. In addition, the kinetics of grain growth under the conditions described in [40] are so fast that controlling grain size would likely become an issue. In this regard, an average grain size of 30 to 100 μm would be ideal, since grains would be large enough to machine micro-cantilever beams within a single grain. Thus, heat treatments at lower temperature were performed first to achieve a ratio of oxygen to metal (O/M) close to 2.1. The heat treatment work was conducted by co-workers H. Lim, R. McDonald and B. Shaffer at ASU. The d-UO_2 sample was provided by Los Alamos National Laboratory (LANL).

After polishing a d-UO_2 sample with O/M ≈ 2 and a relative density of about 95% was heat-treated using a vertical furnace at a temperature of 1200 °C and a pO_2 (partial oxygen pressure) of about $7x10^{-7}$ atm. The heat treatment lasted about 5 hours and the sample was then kept in the furnace for another two and a half hours at the temperature of 1200 °C. Then the system was cooled down slowly for the purpose of avoiding cracks. It was observed that the distribution of grain size did change. However, instead of increasing, the number of grains with large size decreased, as shown in Figure 2.1.

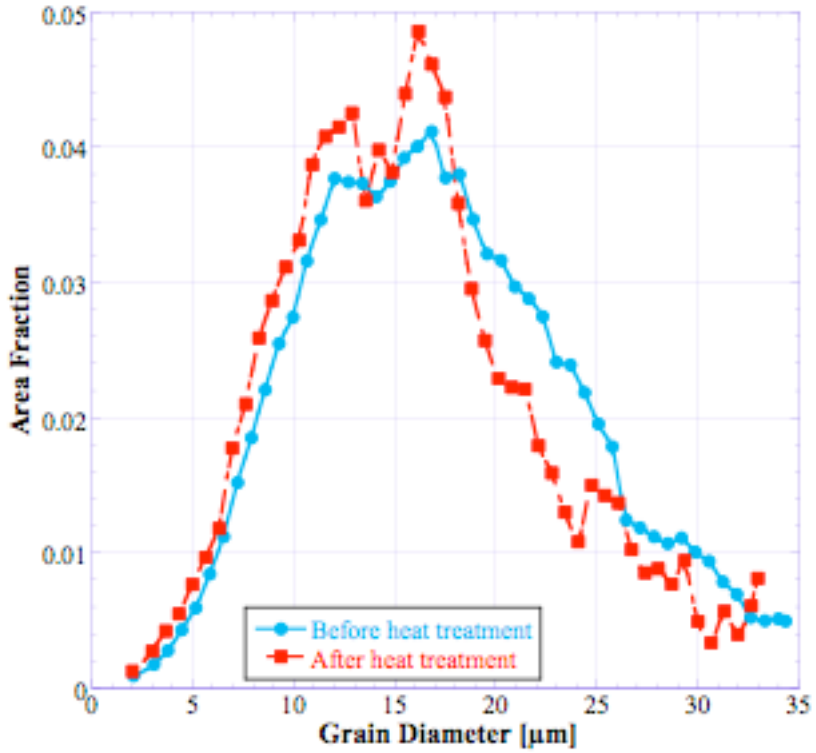

Figure 3.1: Grain size distribution for d-UO_2 before and after heat treatment.

These observations indicated that the condition described just played a role in homogenizing the grain size, instead of increasing average grain size greatly. Therefore, a furnace temperature of 1200 °C is likely insufficient to promote bulk grain growth, particularly given that heat loses from the tube end-caps used led to a temperature difference between the sample and the furnace of about 70 °C. To solve this problem, heat shields made of high-grade stainless steel were used to reduce both radiation and convection heating of the end-caps. Another set of experiments were carried out with sample temperature reached 1200 °C and a $pO_2 \approx 10^{-4}$ atm. At this time, the sample was heated for 48 hours. However, the results were not satisfactory. The average grain size of the sample decreased from 12 um to about 9.9 um. The result indicated that the

conditions used were too close to the boundary between the UO_{2+x} one-phase region and the UO_{2+x}/U_3O_8 two-phase region, as shown in Figure 2.2.

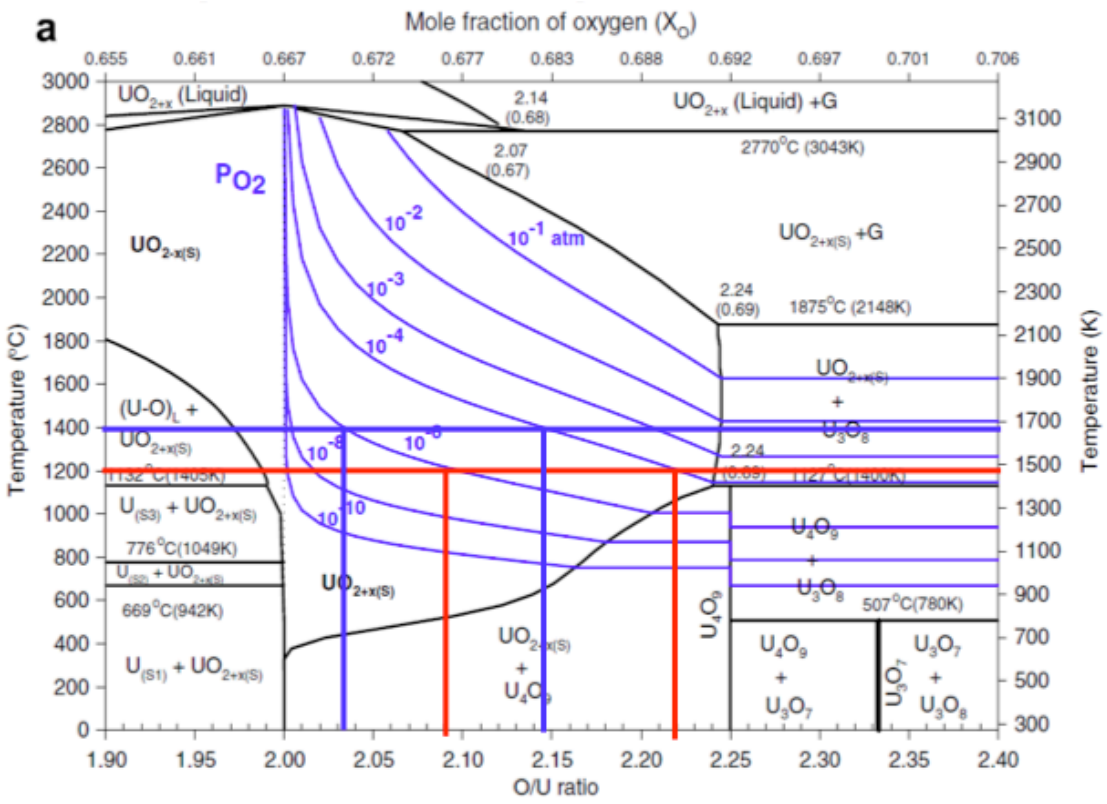

Figure 3.2: Phase diagram of the U-O system [41] showing the expected conditions for several heat treatments. Red lines indicate heat treatments done and blue lines indicate planned heat treatments.

A third set of experiments was performed to try to obtain larger grains. At this time, the gas was a mixture of ultra high purity (UHP) Ar and Ar-100 ppm O_2. The heating process lasted 113 hours at 1215 °C. Ceramography showed that the average of the grain size increased from 10 um to 13 um, which is still not ideal. To improve the results, the nominal temperature was increased to 1460 °C with Ar—5% H_2 and Ar-100

ppm O_2 for 76 hours and at this time, average grain size increased from 13 um to 25 um, which was considered adequate for manufacturing micro-cantilever beams.

3.1.2 Fabrication of Micro-cantilever Beams Using Focused Ion Beam

After heat-treatment, the first batch of samples with average size of 8-10 um was shipped to University of California, Berkeley (UCB) and then grains with appropriate orientation and size were selected to conduct micro-cantilever bending tests at room temperature.

The fabrication of micro-cantilever beams using FIB techniques was conducted at UCB as follows: Firstly, a 7-15 nA beam current was used to cut three trenches, which were about 20-30 um wide and 10 um deep. These cuts formed a U-shaped trench that defined the rough outline of the beam. Then the beam was trimmed using a 1-3 nA beam current. The sample was tilted 45° along the length axis and the base of the beam was undercut from both sides. This operation created the triangular part of the micro-cantilever beam. The manufacturing process can be seen in Figure 2.3.

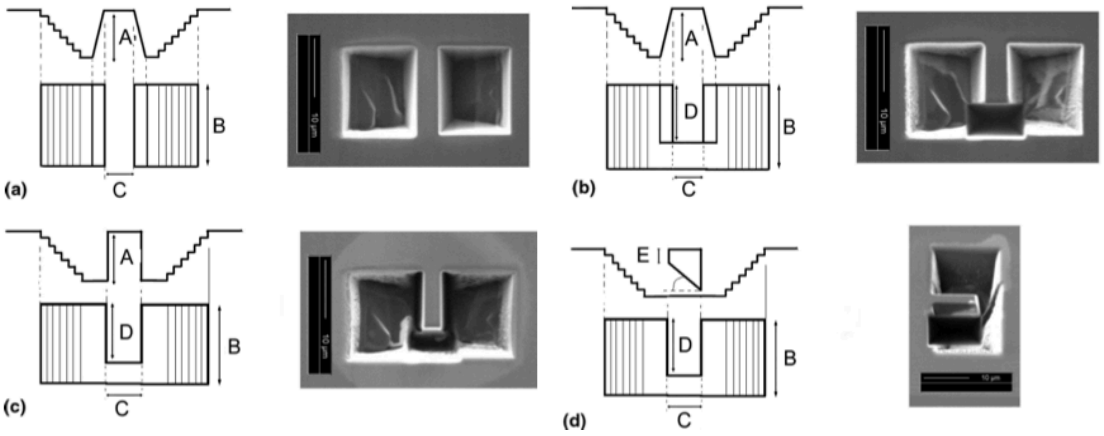

Figure 3.3: Sample preparation process [31].

3.1.3 Micromechanical Testing Procedure

The samples were tested at room temperature. Load-deflection curves for these beams were obtained using a MicroMaterials nanoindenter, which measures the force versus displacement of the tip after it makes contact with the testing material. Indents were then made into bulk UO_2 to measure the indent depth, with the assumption that the same force would produce the same indent depth in the micro-cantilever beams and any additional displacement will come from the micro-cantilever bending. The micro-cantilevers were loaded under displacement control at a constant displacement rate of 10 nm/s until the beam was fractured. One of these curves obtained using a flat punch is shown in Figure 2.4.

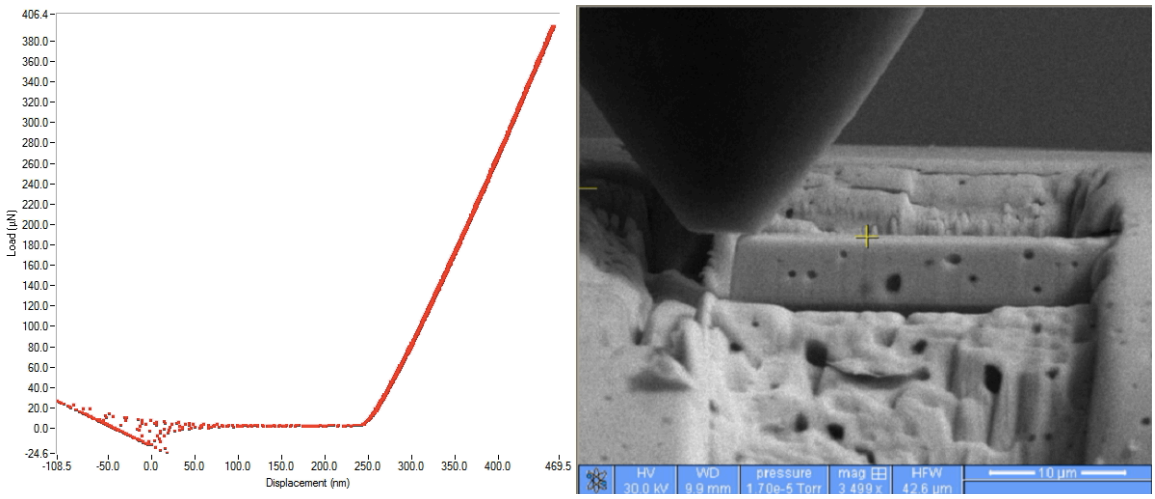

Figure 3.4: Load-deflection curve and an in-situ SEM image of a micro-cantilever beam; this work was conducted in UCB.

3.1.4 Analysis of Load-deflection Data

The data obtained included time, load and displacement at each time; indent depth and the distance from the loading point to the substrate. After removing indent depth from the total depth, the new displacement obtained could be regarded as the displacement from the micro-cantilever bending. Equation (2) and (3) were then used to calculate moment of inertia (I) and vertical distance between neutral plane and upper surface (y). The curve of load-deflection was plotted and the slope of it was obtained. Using equation (1), Young's modulus could be calculated.

3.2 Modeling Procedure

3.2.1 Creating Finite Element Models in Abaqus™

The finite element software used in the modeling procedure is Abaqus™ and the process involved creating parts and assemblies, creating materials and assigning them,

creating steps and meshes, defining boundary conditions and applying loads. Then jobs were created for Abaqus™ to run the corresponding simulations. An outline of the procedure is shown in Figure 3.5.

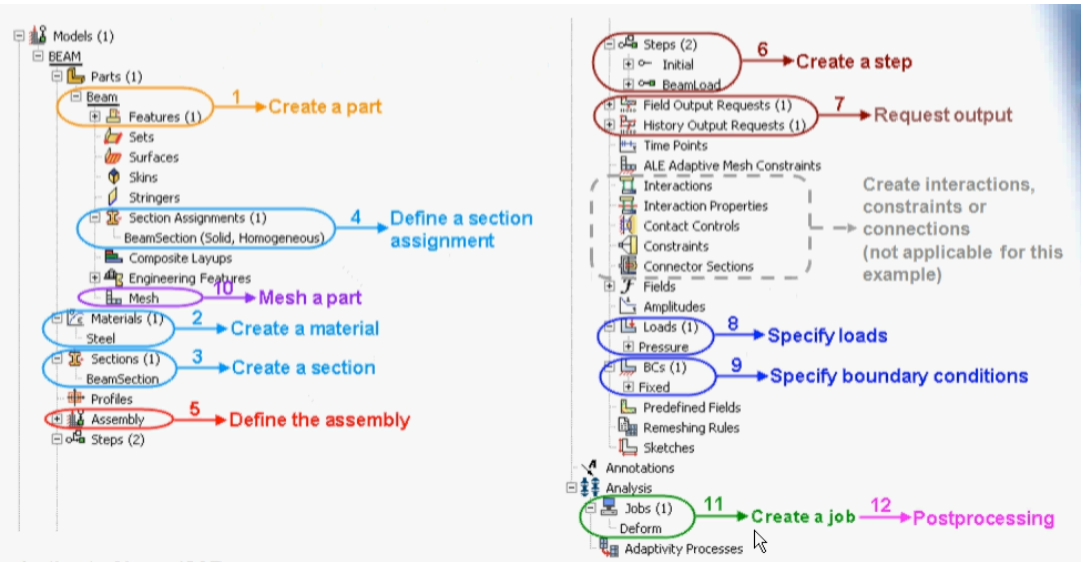

Figure 3.5: Modeling procedure in Abaqus™

3.2.2 Procedures to Create Finite Element Models

The first thing to do is to measure the dimension of the beam and the substrate, including length, width, height of the whole beam and the parallelepiped that can be sued to approximate the substrate. The next thing to do is to determine the system of units used in Abaqus™, since Abaqus™ does not require the user to use the particular system of units, any units can work as long as they are consistent. The most common systems of units are listed in Table 3.1. The system of units selected for the current modeling work has length in mm, force in N, time in s, and stress in MPa. Then a 2D sketch can be drawn in Abaqus™ depicting the cross section of the substrate. After extruding along the

width, a 3-D model is created. The beam is created according to the same process. After the model is created, material properties were defined and assigned to it.

Since the main interest of this work lies in the elastic property of the material, elastic data, which include a value of 219000 for Young's modulus and a value of 0.345 for Poisson's ratio [34] are inputted. The next thing to do is to generate the mesh; the model is divided into two parts, which are the substrate and the beam, to allow mesh generation in each part individually. The element type is an 8 node linear brick.

For each of the cantilevers in the experiments, an FE model was created for the purpose of capturing the specific geometry of the measured dimension. The load is applied whether as a point load or as a pressure on several elements in the middle of the width, with the distance between the center of the region of these elements to the substrate equals to that of the experiment. Pressure was calculated as the ratio of the load to the area of the region. Boundary conditions are that all of the surfaces of the substrate are in encastre, except for the top surface. In this way, the boundary conditions used can capture that of the beams in the experiments.

Table 3.1: System of Units used in Abaqus™.

Quantity	SI	SI (mm)	US Unit (ft)	US Unit (inch)
Length	m	mm	ft	in
Force	N	N	lbf	lbf
Mass	kg	tonne (10^3 kg)	slug	lbf s^2/in
Time	s	s	s	s
Stress	Pa (N/m^2)	MPa (N/mm^2)	lbf/ft^2	psi (lbf/in^2)
Energy	J	mJ (10^{-3} J)	ft lbf	in lbf
Density	kg/m^3	$tonne/mm^3$	$slug/ft^3$	lbf s^2/in^4

3.2.3 Type of the Load Applied to the Beam in Abaqus™

The indenter tip was studied in order to determine the type of the load, i.e., concentrated load on a node, or pressure on a specific area, that should be applied to the model because in some cases, when a concentrated load is applied to a certain node, the stress distribution will become abnormal close to the loading area. According to the data provided by UCB, the average contact depth, which was given by the intercept of the initial unloading slope with the displacement axis [42] was approximately 100 nm. The contacting area was calculated to be approximately 0.245 nm^2 using equation in [43]. Since the contact area was very small comparing to the area of the whole surface, the load could be regarded as the concentrated load on a node. On the other hand, according to Saint-Venant's principle, which claims that the difference between the effects of two different but statically equivalent loads becomes very small at sufficiently large distances from load, a pressure load with equivalent value could also be applied to the same place of the beam to produce the same effect as the concentrated load. In that regard, the type of the load to be applied will be a pressure load.

3.2.4 Measuring Displacement in Abaqus™

The quantification of load-deflection curves from the simulations to compare to experimental results requires obtaining displacement from the model. Since the applied load will possibly cause local indentation, as discussed in the experimental procedures and also in the previous section, which can lead to errors in the deflection measurement, deflections are, therefore, measured at the bottom of the beam at the same distance from the clamp where the load is applied. This reduces errors due to spurious displacements

produced by indentation-like behavior at the point of application of the load. This is illustrated in Figure 3.6

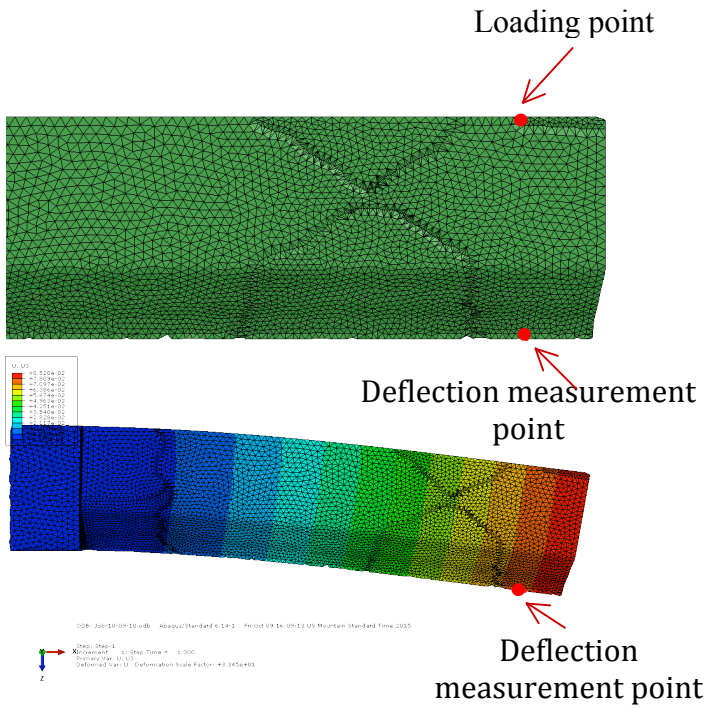

Figure 3.6: The place to measure displacement in Abaqus™ is at the bottom of the beam.

3.2.5 Using Finite Element Models to Determine Young's Modulus

After the model with the same geometry as the beam tested in the experiments had been created, an estimated Young's modulus was inputted and the same force was applied at the same place of the model. Deflection was then measured at the point described in section 3.2.4 and load-deflection curve was plotted. The slope could be calculated and was compared to the one obtained from experimental data. Then, the value of Young's modulus inputted was changed until the slope of the load-deflection curve

was the same as that obtained in the experiment. The current Young's modulus would be regarded as the one determined using finite element analysis.

3.2.6 Simulation of Anisotropic Properties of UO_2

Due to the fact that UO_2 is anisotropic and that the grains of the initial samples were not large enough to allow micro-cantilever beams to be fabricated in a single grain, these beams had to be manufactured in a few grains, all of which may have different orientations and elastic properties. To take into account different anisotropic properties of the different grains inside the beam, the model was divided into several parts, where each of them represents one grain. A typical EBSD result for a single grain within a beam is shown in Figure 3.7, where Euler angles are used to calculate elastic constants and the X vector, which indicates the crystallographic direction parallel to the axis of the beam, is used to calculate Young's modulus of the grain once it is normalized as a unit vector.

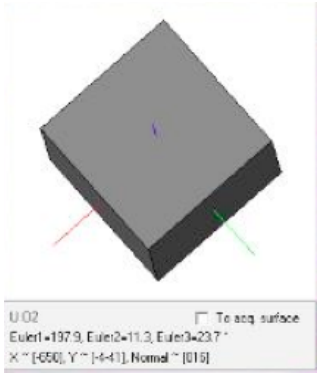

Figure 3.7: A typical result obtained from EBSD showing the orientation of the grain.

Using Euler angles taken from EBSD, anisotropic elastic constants could be extracted for a coordinate system parallel to the axes of the beam, using the rule to rotate

rank-4 stiffness tensors [23]. Then, these parameters were imported into the material defining window in Abaqus™, thus, anisotropic material properties could be created and assigned to different parts, which can be seen in Figure 3.8.

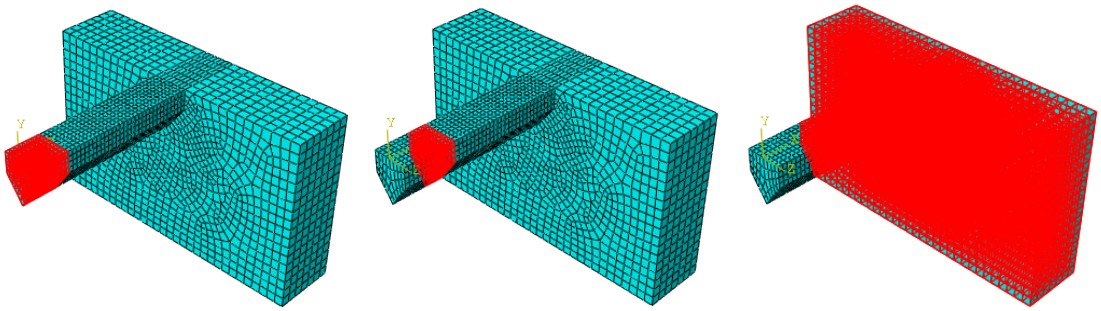

Figure 3.8: Model divided into 3 parts representing 3 different grains.

After the simulations are conducted using a monolithic model, i.e., no pores, it is necessary to perform simulations to account for the effect of porosity, which is likely to reduce the values of elastic moduli significantly, as compared to that of the matrix. This is described in the next section.

3.2.7 Simulation of Pores in HyperMesh™ and Avizo™

As described in the literature review, the effect of porosity on elastic properties can be stronger than what one would expect based on linear effects, i.e., rule of mixtures. In addition, given that pore size and spacing are commensurate with the dimensions of the micro-cantilever beams, large pores, as compared to the cross section, should have a large effect on the moment of inertia during bending, so these effects need to be studied. In that regard, two approaches are used to perform this study.

The first method involved a model built with the typical geometry of a fabricated micro-cantilever beam using Abaqus™. This model (shown in Figure 3.9) was first imported into HyperMesh™ and some cleanup of the mesh was conducted to make the element size as uniform as possible in the beam region. Then, the mask tool in this software was used to conceal the parts of the model that did not need to be modified and the delete tool was used to remove elements to produce pores. The volume of the elements removed was calculated according to porosity (5% in this case) and the volume of the beam. The size of each pore remains the same and they are randomly located along the beam. After deleting elements, the model was imported into Abaqus™ for further analysis. It is expected that effective (apparent) Young's modulus measured from the load-deflection curve will decrease after elements are removed from the beam.

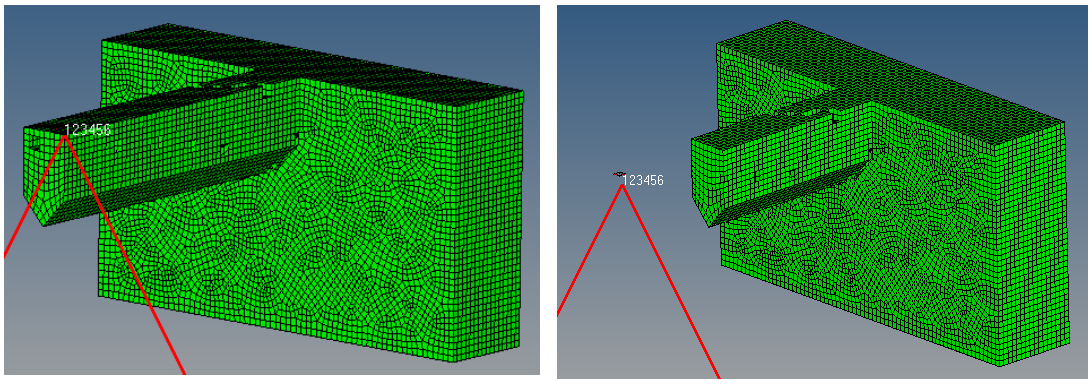

Figure 3.9: A part of the beam is masked in HyperMesh™.

The second approach involves evaluating effects of porosity from actual samples. This requires microstructure reconstruction of micro-cantilever beams in UO_2. Images of the cross section along the height of the beam (Figure 3.10(a)) were collected in UCB

with 3-D serial sectioning techniques using FIB and EBSD. The beam was sliced and scanned about every 1 um and the raw images shown in Figure 3.10 (b) were obtained. These images were pre-processed first and then imported into the commercial software Avizo^{TM} for microstructure reconstruction. The pre-processing includes splitting, cropping and size modifying and the importing process involves using the Avizo Stacked Slices Tool, since the thicknesses of each layer were not identical. Images were then segmented and labeled (Figure 3.10 (b)) based on the grain boundaries that could be seen in the images. Since there were just 7 layers, the accuracy on the size of the individual pores is likely medium to low, but it was considered enough at this stage to study general effects. Nonetheless, Avizo^{TM} allows interpolating the geometry between layers, which helps to make the boundary between different grains and between pores and the matrix as smooth as possible. Once this is done, the surface is generated. One of the advantages of Avizo^{TM} is that it generates 2-D meshes at grain boundaries and generates 3-D meshes at other places. Then a tetrahedral grid is generated based on the surface mesh. The finished reconstruction is shown in Figure 3.10 (b) and the volume of pores is estimated to be 2.5%, which is just half of the expected porosity. The discrepancy might be related to the fact that the number of layers obtained from slicing was too low to resolve all the pores present; hence, many pores were neglected during the process, and that the small size of the beams is likely to lead to variations on the local volume fraction, particularly given the fact that micro-beams are often machined in regions with low observable porosity, in an effort to reduce the effects of this variable.

(a) 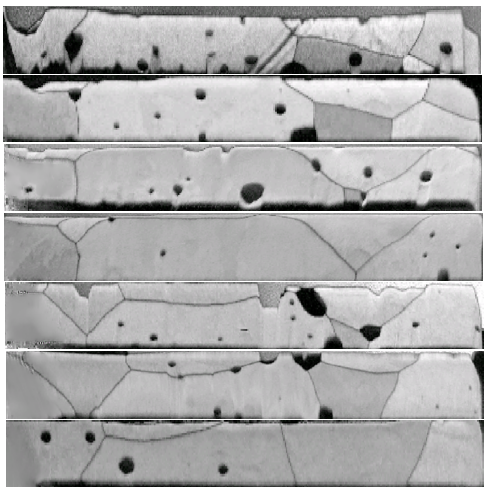 (b) 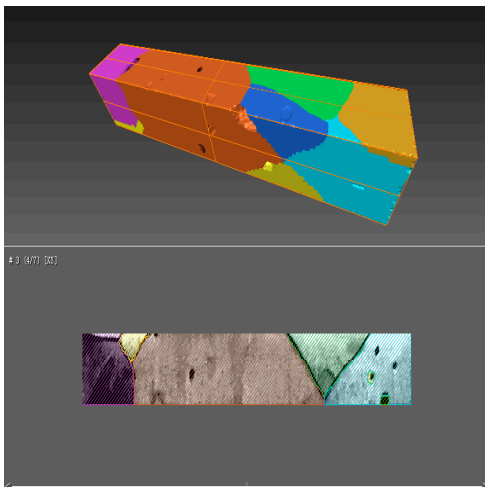

Figure 3.10: (a) Raw images collected using FIB at UCB; (b) Reconstructed model in Avizo™.

In order to add substrate to the beam, margins were added to three sides (Left, upper, bottom) of the 7 images. The same process, which includes segmentation, labeling, interpolation, generating surface and meshing was repeated. The only difference was that a new label containing the substrate was added.

The element type for the mesh produced in Avizo™ was linear tetrahedral, which is fairly stiff and often leads to wrong answers for bending-dominated problems. However, since tetrahedral elements can be used to mesh any 3D volume, regardless of shape or topology [44], it is the default element type in Avizo™. In order to make sure that the finite element results are accurate and the solution is converged, a comparison was carried out between displacements obtained from the model using tetrahedral elements (model 1) and the model using incompatible brick elements (model 2). The number of elements in model 1 is 33878 and that of model 2 is 45822. The results are listed in Table 2.2, which shows that although the number of elements in model 1 is

smaller than that of model 2, when the same load is applied to the same locations of these two models the results are almost the same. Since incompatible brick models can be regarded as reliable for bending dominated problem, the results of the model using tetrahedral elements in this case can also be regarded as accurate and convergent.

Table 3.2: Load and displacement data for the same model using different mesh element.

Load (N)	Tetrahedral elements (μm)	Incompatible brick elements (μm)
0.01	3.48E-03	3.48E-03
0.02	6.96E-03	6.95E-03
0.03	1.04E-02	1.04E-02

IV RESULTS AND DISCUSSION

4.1 Size Effect of Substrate

Since the grain size of the first samples tested was small, the first set of micro-cantilever beams were manufactured with a back-to-back geometry, i.e., two beams were placed together with a substrate between them (Figure 4.2), for the purpose of putting as many as beams inside the occasional large single grain that could be found in the microstructure of those first samples. The load-deflection curve of one of the beams is shown in Figure 4.1, the slope of which is 10484 N/m. Using the beam theory introduced in Chapter I, one can get Young's modulus of 109 GPa.

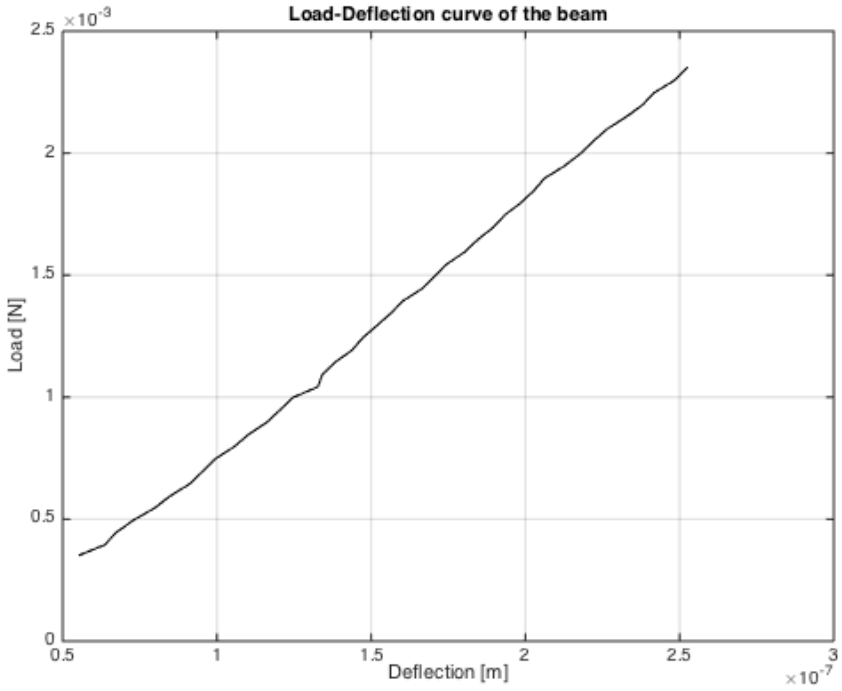

Figure 4.1 Load-deflection Curve of the Beam with Back-to-back Geometry.

However, the result is 254 GPa using finite element method. By contrasting the model before and after the load was applied, it is found that both the substrate and the beam on the other side showed a deflection. Since the substrate deflected, the displacement measured will be larger than it should be, which means that the slope of load-displacement curve is underestimated. Since Young's modulus is positively correlated with the slope, Young's modulus is underestimated too. Hence, the calculated Young's modulus was greatly lower than finite element result. It is also noticed that the substrate between two beams is narrow and will be hard for it to remain fixed while load is applied close to it.

In order to find out the minimum size of the substrate model that needs to be used to account for its flexibility in the finite element simulations, the following models (Figure 4.3) were created. Each of these three models has the same size of the beam, but different size for the substrate. The width of the beam and the width of the substrate are both 10 um for model 1, while the width of the substrate for model 2 is 20 um and that of model 3 is 30 um. The same load was applied to the same place of the beam and the boundary conditions are as described previously. The results are listed in Table 4.1, from which we can find that displacements are different between model 1 and model 3 while almost the same for model 2 and model 3. The results indicate that the width of the substrate should be at least larger than that of the beam and it is enough if the width of the substrate can be twice that of the beam.

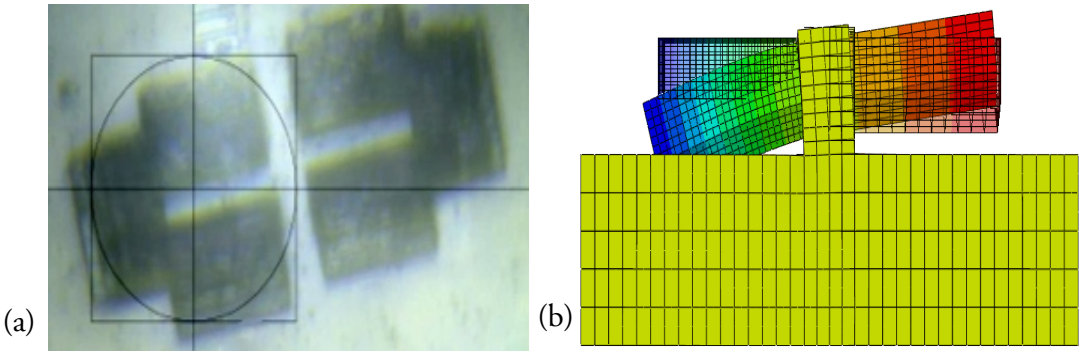

Figure 4.2: (a) Back-to-back geometry; (b) deflection at substrate and the other beam.

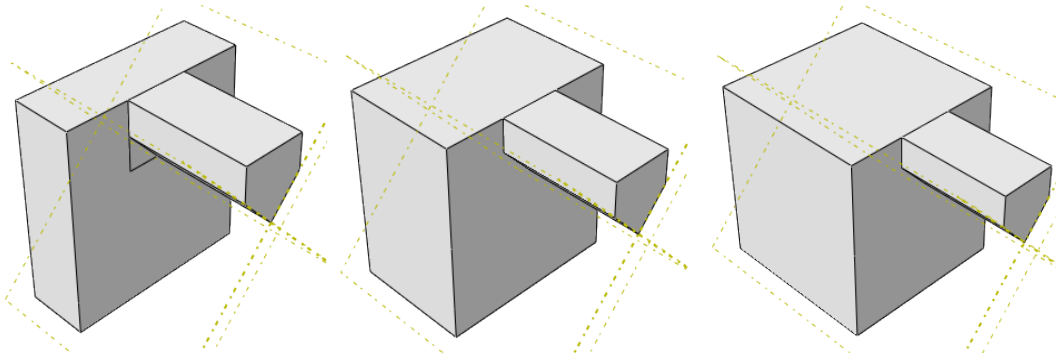

Figure 4.3: Three models with the same size of beam and different size of substrate.

Table 4.1: Displacements for three models that have the same size of the beam and different size of substrate.

Load (N)	Model 1 (μm)	Model 2 (μm)	Model 3 (μm)
0.006	1.71e-4	1.76e-4	1.76e-4
0.12	3.42e-4	3.52e-4	3.53e-4
0.18	5.13e-4	5.27e-4	5.29e-4

On the other hand, even if the substrate is large enough, the distance between the loading point and the substrate can also be an important issue that would influence the value of Young's modulus obtained [30]. According to this reference, when the loading

point approaches the substrate, Young's modulus calculated will decrease and the error will increase. This is likely due to the fact that the displacement caused by the deflection of the substrate can hardly be ignored when the loading point approaches the substrate. It is known from beam theory that displacement of a cantilever beam on a flexible substrate can be divided into [30]:

$$\delta = \frac{PL^3}{3EI} + \frac{PL^2}{k_\theta} \tag{7}$$

and can also be written, assuming a rectangular cross section, as

$$\delta = A(\frac{L}{H})^3 + B(\frac{L}{H})^2 \tag{8}$$

While L decreases, the difference between these two terms becomes smaller and the second term cannot be ignored and simple beam theory cannot work properly anymore. Hence, it is very important to have a large value of L/H. Since the grain size was small for the first samples, it was hard to fabricate a beam with a length large enough to get an appropriate value of L/H.

Given the uncertainty and the inaccuracy introduced by a low value of L/H, it can be problematic to match the calculated load-deflection curves to experimental values. Since Young's modulus depends greatly on the slope of load-deflection curve, the calculated Young's modulus can be inaccurate.

4.2 Effect of Elastic Anisotropy and Equivalent Young's Modulus

Six additional micro-cantilever beams were fabricated at UCB, and five of them were studied using micro-cantilever bending testing. Due to the deflection at substrate observed in the back-to-back geometry and the inaccuracy it introduced in the calculation of Young's modulus, this geometry is not selected in the new set of experiments. At this time, single micro-cantilever beams were fabricated. One of the beams tested is shown in Figure 4.4. The dimensions of all the beams fabricated and tested are listed in Table 4.2.

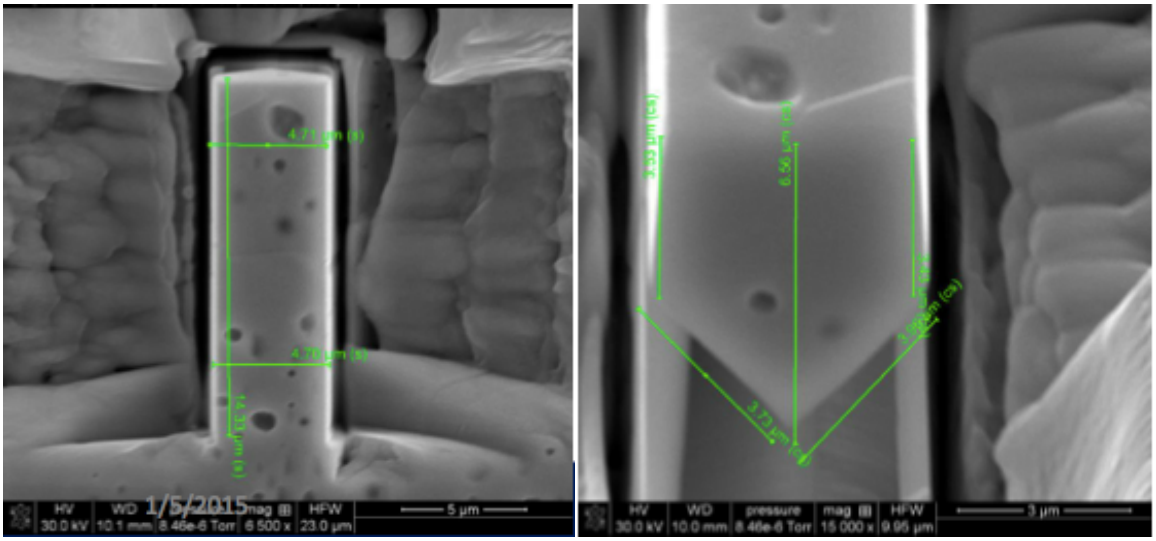

Figure 4.4: One of the micro-cantilever beams manufactured at UCB.

Table 4.2: Geometry and Young's moduli estimates from five micro-bending tests.

Sample #	Whole length (μm)	Loading location (μm)	Width w (μm)	Height b (μm)	Whole height H (μm)	L/H	Slope (μN/nm)	E (GPa)
Beam 1	21.2	18.90	4.33	2.38	5.13	4.13	1120	141
Beam 2	20.4	17.71	3.42	3.50	6.06	3.37	1680	123
Beam 3	19.9	16.38	4.30	2.25	5.33	3.74	1538	93
Beam 4	20.8	17.00	3.64	2.74	5.54	3.75	2025	198
Beam 5	28.5	27.04	3.99	5.27	7.48	3.81	1915	147

Although the ratio of L/H is not too small, Young's modulus of these five beams is still lower than that of the polycrystalline, fully dense UO_2, which is approximately 219.6 GPa [34]. Young's modulus of beam 4, which is the biggest one among all of these beams, is still almost 10% lower than the reported value.

Note from the EBSD result (Figure 4.5) that beam 5 consisted of several different grains with different orientations.

Figure 4.5: EBSD result showing different orientation of the grains in beam 2.

Since the size of the grains was still not large enough to allow micro-cantilever beams to be manufactured into one single grain, they have to be fabricated in several grains instead. The properties of the combination of grains with different orientations can be totally different from any of the individual grains. In that regard, Effective Young's modulus should be considered to account for different orientations of different grains and

the material anisotropy. One simplifying assumption that can be made is that the arrangement of grains is similar to a bamboo structure, as shown in Figure 4.6.

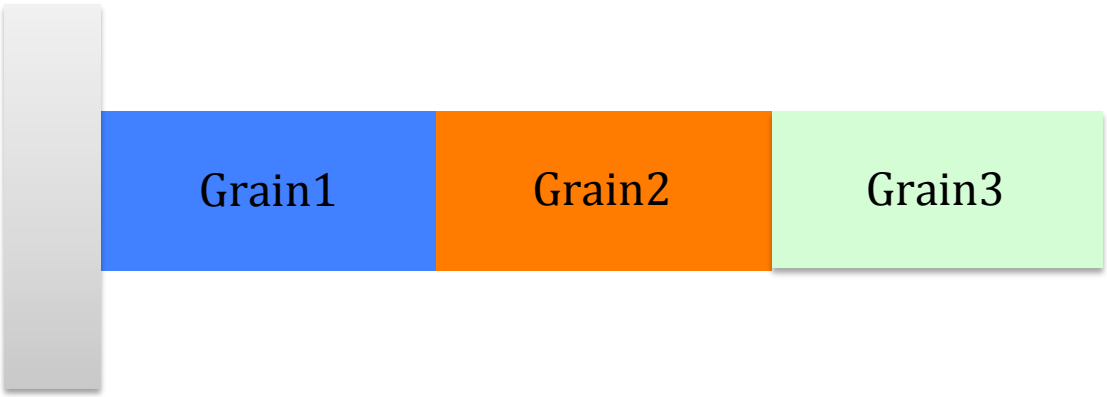

Figure 4.6: Schematic graph showing the assumed 'bamboo structure' for multicrystalline beams.

For beams that have a structure like that shown in Figure 4.6, it is possible to find an analytical relationship between Young's modulus of each grain, the length of it, and the distance between it and end of the beam. The resulting relationship is shown in Eq. 9 and it was obtained using an analysis from beam theory:

$$\bar{E} = \left(\sum_{1}^{n} \frac{(L_i/L)^3 - (L_{i-1}/L)^3}{E_i}\right)^{-1} \quad (9)$$

Where $\bar{E}$ is equivalent Young's modulus, L_i is the length from the end of the beam to the beginning of the grain, L_{i-1} is the length from the end of the beam to the end of the grain, L is the total length of the beam and E_i is the Young's modulus of each

single grain. A first simple case is to assume that the beam consists of 2 different grains, with Young's moduli of 100 GPa and 200 GPa. If these 2 grains have the same length and the grain with larger Young's modulus is close to the substrate, then the effective Young's modulus for the beam is about 180 GPa, which is just 20% lower than the grain close to the substrate, instead of 50% as one might have first expected. On the other hand, if the Young's modulus of the grain close to substrate is 100 GPa and the other one is 200 GPa, then the effective Young's modulus is ~107 Gpa, which is just 7% above 100 GPa. These results show that the value of Young's modulus for the beam is strongly dominated by the value of Young's modulus of the grain close to the substrate. Plots of effective Young's modulus versus the length fraction (the ratio of the length of the grain close to the free end to the whole length of the beam) can be obtained from Eq. 9 for these two cases, as shown in Figure 4.7. It can be concluded that the value of effective Young's modulus obtained from bending is dominated by the behavior of about one half of the beam close to the substrate.

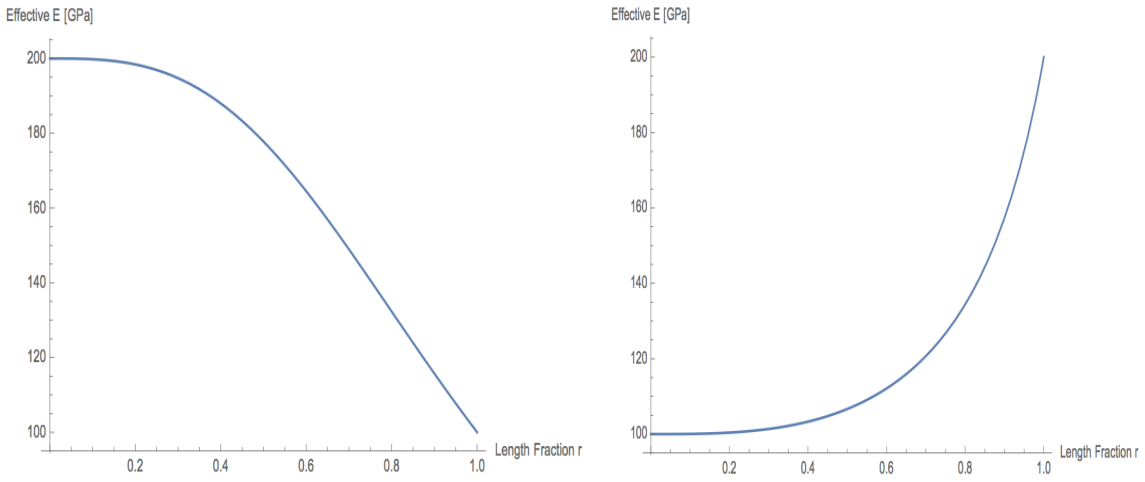

Figure 4.7: Plot of effective Young's modulus with the length fraction when the beam is consisted of 2 grains with different Young's modulus.

The results obtained from beam theory, finite element method and using Eq. (9) are listed in Table 4.3.

Table 4.3: Comparison of Young's moduli results using beam theory, finite element method and effective Young's modulus equation. All values in GPa.

Sample #	Beam theory	Finite Element	Calculated using equation (9)
Beam 1	141	183	168
Beam 2	123	201	212
Beam 3	93	197	197.8

Results obtained from finite elements are very close to those obtained using the effective Young's modulus equation, which demonstrates that this equation works well to predict Young's modulus of the bamboo structure. However, there are also drawbacks

using the effective Young's modulus equation. First of all, grains actually have to be arranged in the bamboo structure, which is not always the case. Secondly, this method can only take into account grains that can be detected by EBSD, which means internal grains will be ignored and errors will be introduced as a result.

Furthermore, the UO_2 samples used to fabricate the beams had a random texture, so no preferential orientations towards <111>, in which direction the value of Young's modulus is minimum, were present to produce a strong bias of the results towards lower values of Young's modulus. Even if the sample had been single grains oriented along <111>, Young's modulus would be 163.5 GPa, which fails to account for four values in Table 4.2 that are lower than 163.5 GPa. One can use porosity corrections to check the potential effect of porosity. The equation proposed in [34] is shown in equation (5).

$$E' = 219.6e^{-3.025P} \tag{10}$$

Where *E*' is the corrected Young's modulus in GPa and P is pore fraction. Using *P*=0.05 one can obtain *E*'=188.7 GPa. But the discrepancy is still so large that only one of the beams shown in Table 4.2 has a Young's modulus higher than this value. If the sample had been a single grain oriented along <111>, as assumed above, 5% porosity will lead to a Young's modulus of 140 GPa, which still cannot explain the two lowest values in Table 4.2. However, part of the scatter is undoubtedly related to the small number of grains contained in the samples, but these preliminary estimates strongly suggests that grain orientation effects are not the only reason for the lower values of E shown in Table 4.2.

Another important factor is the presence of porosity, particularly since individual pores can represent a meaningful fraction of the cross section of the beams (see Figures 4.8 and 4.9). This precludes the possibility of modeling the beams as homogeneous with an "effective" modulus given by the corrections proposed in [31, 33]. According to beam theory, these large pores can have significant effects on the moment of inertia of a given cross section, particularly when they are located close to either the top or the bottom surface. This, in turn, can lead to significant reductions on the value of the slope, as can be deduced from equation (1), and a subsequent reduction in the Young's modulus estimated from the load-deflection data. The sample shown in Figure 4.8 also shows that pores can be present in small clusters of 2 or 3 pores close together, which is a situation hard to model using analytical approaches; therefore, FE models were created to study these effects, as described next.

4.3 Study of Effect of Pore Location

Beam 5 was used for the purpose of conducting 3-D serial sectioning and microstructure reconstruction. This beam is shown in Figure 4.8. In this experiment, the test was performed in-situ in the SEM to allow for accurate placement of the indenter and the accurate measurement of the distance between the point of application of the load and the substrate during testing. Testing in-situ inside the SEM also made it possible to observe the testing process. In the test, the indenter tip was a 5 um flat punch, instead of the Berkovich tip used in previous tests. The tip started about 200 nm above the micro-cantilever beam and then the tip moved down to press the beam, which can be observed

in Figure 4.9. It can also be noticed that the load-displacement curve is completely linear during the whole testing process, once load started deviating from zero.

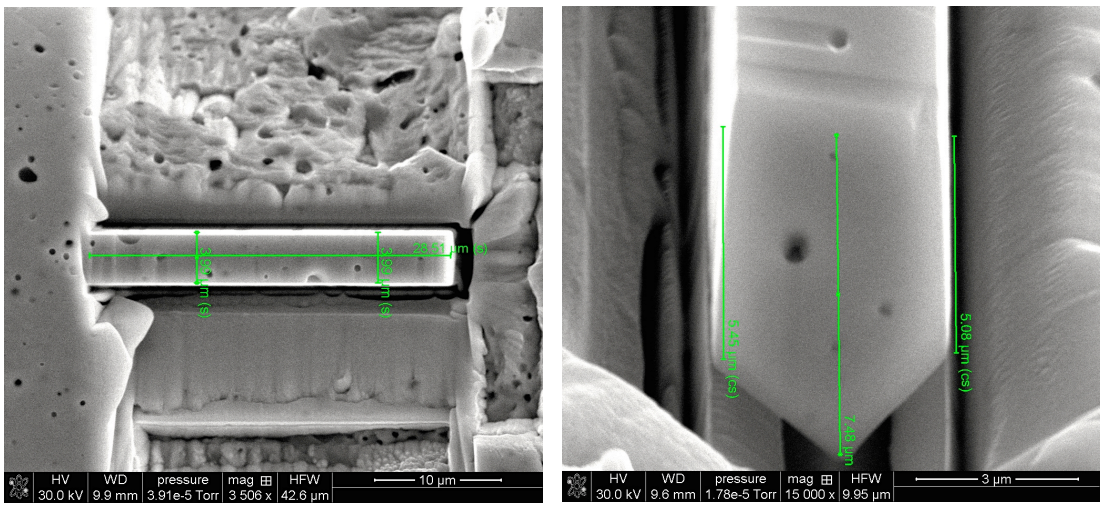

Figure 4.8: The beam used to conduct microstructure reconstruction.

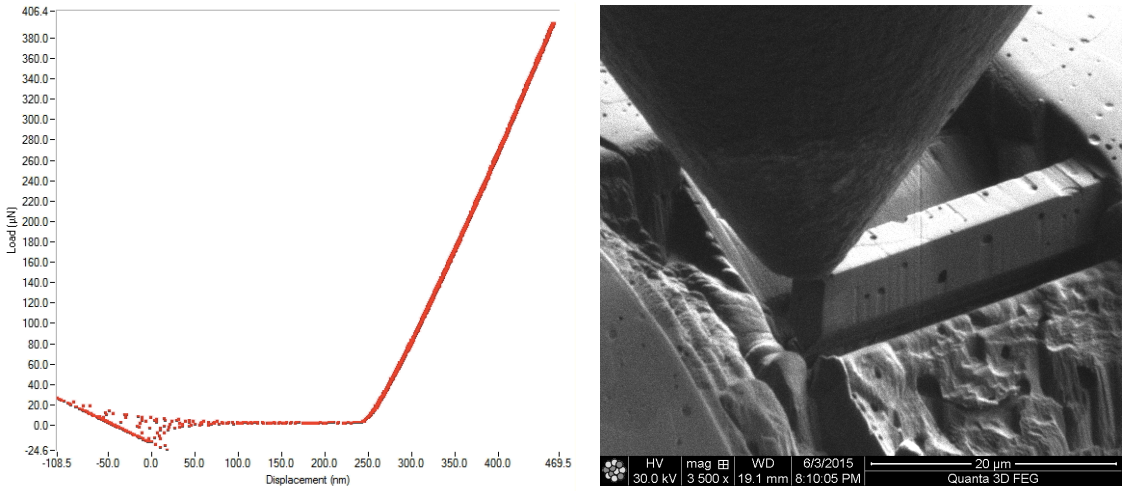

Figure 4.9: The load-deflection curve and an in-situ SEM image of a micro-cantilever beam. The scale bar in the SEM picture is 10 µm long. This work was conducted at UCB.

After the test, the load-displacement curve was plotted and the slope of it is 1914.6 N/m and Young's modulus was calculated to be 147 GPa, which is 32% less than the reported value for isotropic, polycrystalline UO_2. To verify the result, ultrasonic pulse measurements were conducted at ASU by Robert McDonald to measure Young's modulus for bulk UO_2. In this test, the density of the sample (10.733 g/cm^3) was slightly different from the one use to conduct micro-cantilever bending tests (10.58 g/cm^3). The thickness of the sample and the time of flight were measured and recorded, as shown in Table 4.4. Since both of the values measured in the bending test and using the ultrasonic pulse method are lower than the reported value, something else needs to be considered to explain the phenomenon.

Table 4.4: Parameters and Young's modulus measured in ultrasonic pulse method.

Sample thickness (mm)	Time of flight (μs)	Sound Velocity	Young's modulus
2.570	1.024	5.020	169.580

By observing SEM images of the micro-cantilever beam, it is found that there were many pores in uranium dioxide samples and some of the pores were large as compared to the size of the beam, as shown in Figure 4.10.

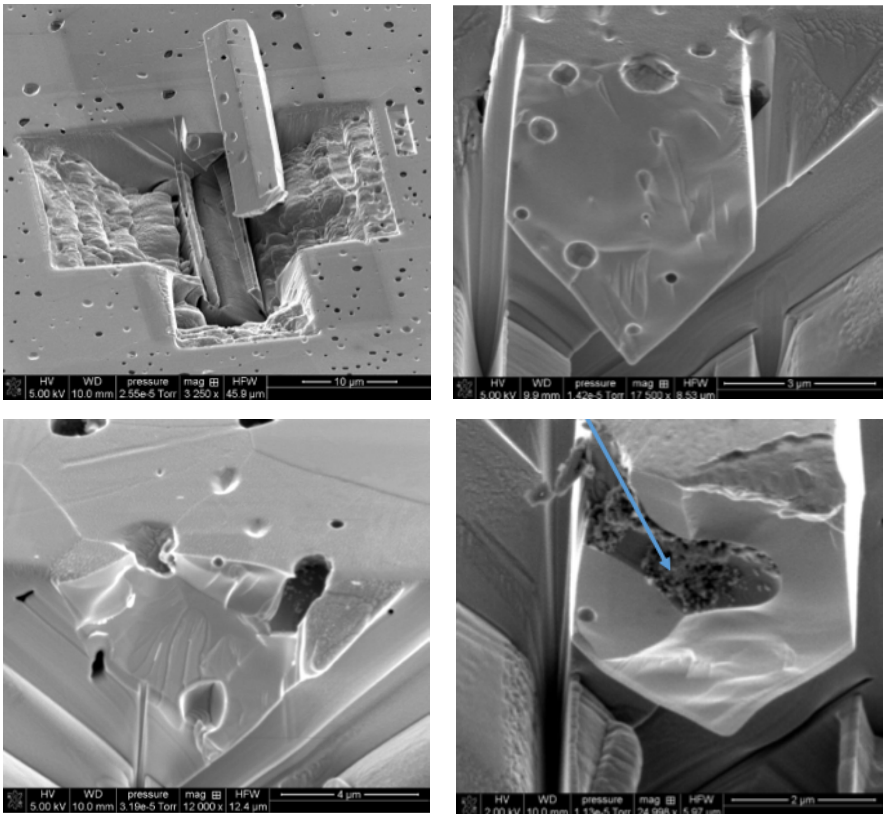

Figure 4.10: Pores at the cross section of the beam.

To understand the effect of pores, some elements of the meshed model were removed using HyperMesh™ to simulate porosity, as described in section 3.2.7. Pores were randomly located in the beam and the volume of pores is calculated according to porosity and volume of the beam. The pores were randomly located in the beam. The porous model was then imported into Abaqus™, where the same load was applied to the same location of the solid and porous beams. Results are listed in Table 3.5. Since the geometry of these two beams remains the same, the slope is the right parameter to compare. The slope of the porous beam is 13% less than that of the solid beam, which means that Young's modulus of the porous beam decreased 13% due to the porosity of 5%. The reduction in Young's modulus obtained in the simulation is close to 14% that is

calculated using equation (4) for the same porosity of 5%, which demonstrates that porosity will indeed lead to the reduction of Young's modulus.

Table 4.5: Load-displacement data obtained in Abaqus™ for the model with some of the elements removed in HyperMesh™

	Solid Beam			Porous Beam		
Load (N)	0.005	0.01	0.015	0.005	0.01	0.015
Displacement (μm)	0.0013	0.0026	0.0039	0.0015	0.003	0.0045
Slope for Compliance	0.3847			0.3349		
Difference				12.95%		

Another phenomenon found in the modeling process was that when elements in different places were deleted, the reductions of apparent Young's modulus obtained from the load-deflection curves were different. For example, when more elements close to the substrate were deleted, there would be a greater reduction of Young's modulus. According to the description in Section 4.2, the grain close to substrate has more weight in determining equivalent Young's modulus, so a similar effect is likely to be at play here.

This was studied further in actual beams used in experiments; microstructure reconstruction was performed with images collected from 3-D serial sectioning using FIB and EBSD at UCB. The actual thickness for each layer obtained from serial sectioning was respectively 0.71 μm, 1.34 μm, 0.76 μm, 0.52 μm, 0.58 μm, and 1.17 μm. Then a new set of models was built, which resembled the beam used in the experiments as closely as possible given the level of resolution used. The procedure is described in detail in Chapter III. This set contains 4 models, one of which is solid and the other three contain pores with the same volume fraction. The only difference among the 3 models

with porosity is that the biggest pore found in the reconstruction was located at different places within the beam. These four models are shown in Figure 4.11, which shows the solid model, the other three figures show models with the biggest pore located close to substrate, in the middle and at the end separately. The volume of pores was kept 2.5% for all three models and the pore inside the yellow circle is the biggest one, and was moved to different locations to study the effects of pore position, as mentioned above.

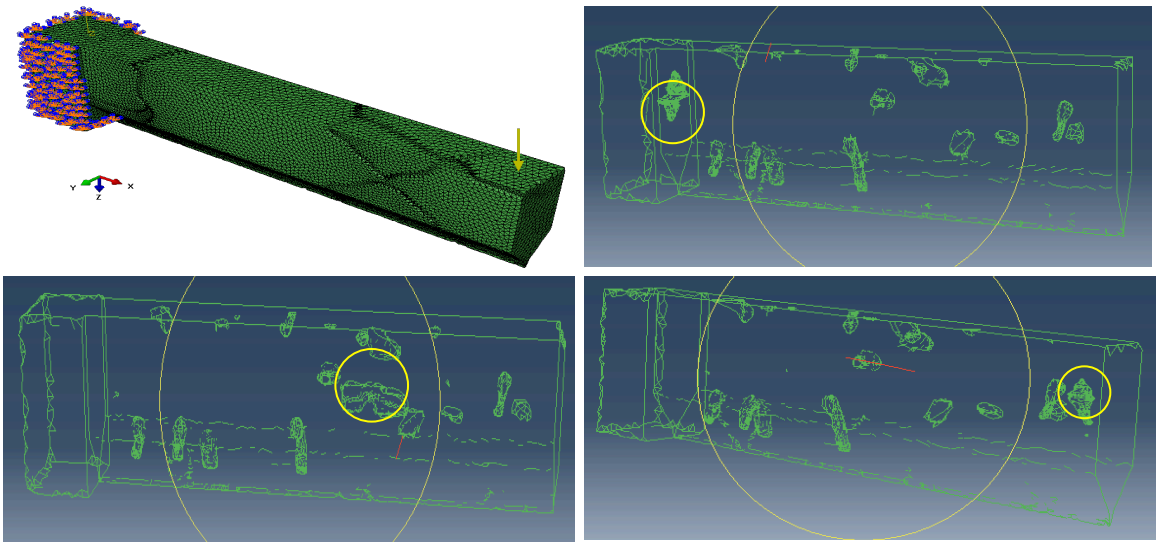

Figure 4.11: Models with pores located at different parts of the beam: (a) solid beam with no pores (model 1); (b) beam with the big pore close to the substrate (model 2); (c) beam with the big pore in the middle part (model 3); (d) beam with the big pore close to the free end (model 4).

Models were meshed with tetrahedral elements to facilitate including the geometry of the porosity and of the grains of the beam that was serial-sectioned. The latter will be used in future studies. Model 1 has about 880900 elements, whereas models

2 through 4 have approximately 730000 elements. A convergence study was conducted as described in Chapter III, given that the tetrahedral elements used are stiffer than hexahedral elements, and solid elements in general can have difficulties capturing bending when using coarse meshes. The beams were subjected to loads of 50, 100, 150 and 200 uN and deflections were measured at the bottom of the beam at the same distance from the clamp where the load is applied. This reduces errors due to spurious displacements produced by indentation-like behavior at the point of application of the load. A Young's modulus of 219 GPa was used for the UO_2 matrix in all cases and results are shown in Table 3.6.

Table 4.6: Load-displacement data obtained in Abaqus™ for the model with one big pore moving from substrate to the middle and to the end of the beam.

Model No.	50 μN	100 μN	150 μN	200 μN	Slope	E (GPa)	%
No Pore	1.89E-02	3.78E-02	5.68E-02	7.57E-02	2640	2.19E+05	
Pore_substrate	2.37E-02	4.74E-02	7.10E-02	9.47E-02	2113	1.75E+05	20%
Pore_middle	2.07E-02	4.15E-02	6.22E-02	8.29E-02	2412	2.00E+05	8.6%
Pore_end	2.02E-02	4.04E-02	6.06E-02	8.08E-02	2475	2.05E+05	8.6%

From Table 4.6 we can see that although a constant void fraction was kept, the position of the pore along the length of the beam plays a significant role in determining the value of effective (apparent) Young's modulus. The largest effect occurs when the pore of interest is close to the substrate, where a reduction of 20% on E is obtained with respect to the case with no pores, which is much larger than the 7% reduction predicted by the equation proposed in [34] for 2.5% pore fraction. This is most likely due to the fact that the cross section of the pore is big, which greatly reduced the moment of inertia

at the substrate. This, in turn, implies that the stresses and strains, which are already large close to the clamp, will be further amplified by the decrease in inertia, leading to larger slopes close to the clamp. This, in turn, can produce a larger arc at the point of application of the load. Local deflections will also be larger, adding to the overall deflection at the end of the beam. Table 4.6 shows an increase of 25% in deflection for the model with pores close to substrate with respect to model 1, in agreement with this interpretation.

In order to further study the effect of the distribution of the pores, three models with pores located in clusters were created and tested. The beams were divided into three parts with equal length, and then pores were placed into one of these three parts, respectively. The first model has no pores, to use the results as a reference. The second model has pores concentrated in the section close to the substrate, the third model has pores located in the middle part of the beam, and the fourth model has pores at the end of the beam. Pores were arranged in the same pattern among all of the models to simplify comparisons. To make the simulated pores representative, the size of the pores was calculated according to the overall porosity from the UO_2 used, the number of the pores and volume of the beam. However, to simplify the models, the overall porosity is still kept at 2.5% in all three cases. A point load was applied on the top surface at approximately 22.9 um from the clamp, following experimental values. The substrate of the beams was modeled as a rectangular parallelepiped with dimensions slightly larger than the cross section of the beam and constrained with zero displacements on all surfaces except at the top. The arrangement of the pores for all cases and the boundary conditions for them are shown in Figure 4.12.

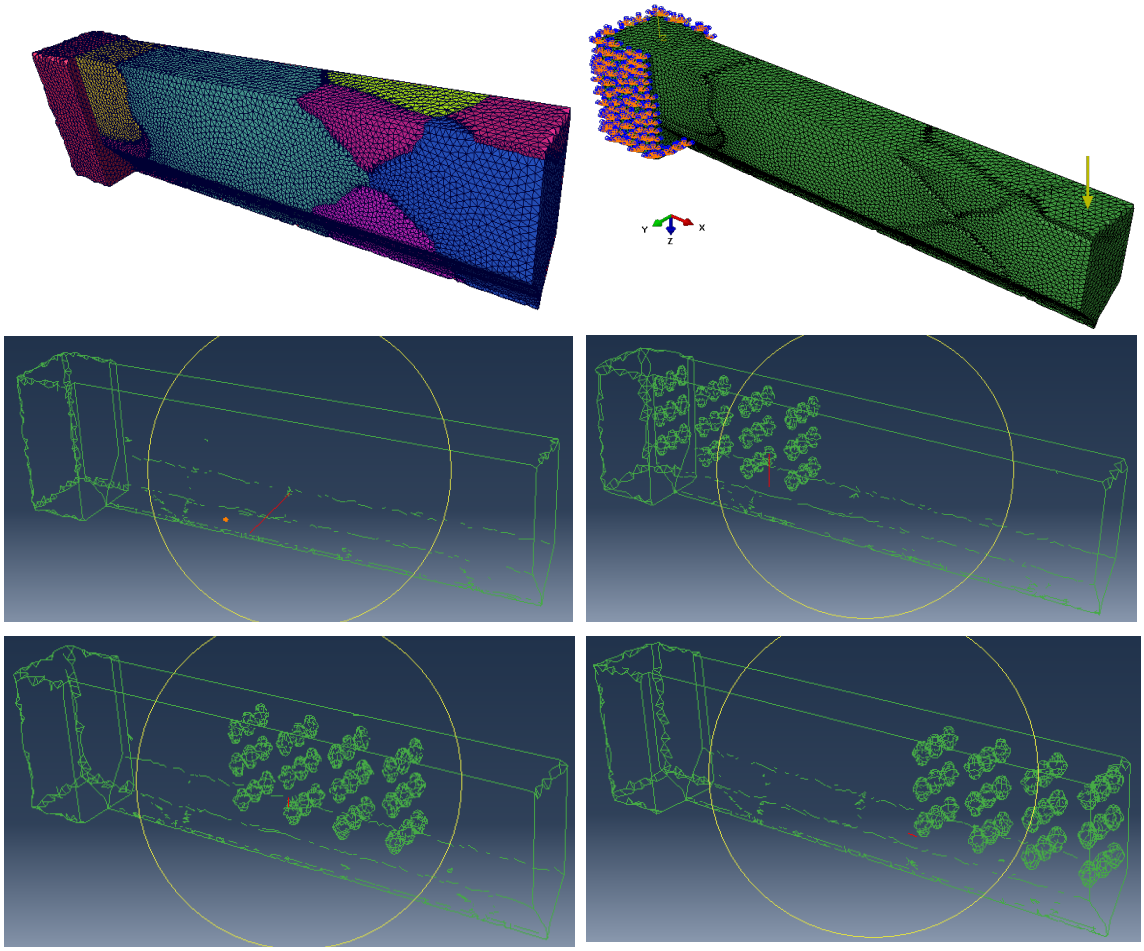

Figure 4.12: Models with pore clusters located at different parts of the beam: (a) solid beam with no pores; (b) The mesh and the boundary conditions; (c) solid beam with no pores (model 1); (d) beam with pores close to the clamp (model 2); (e) beam with pores in the middle of the beam (model 3); (f) beam with pores close to the free end (model 4).

Models were meshed with tetrahedral elements as done with previous models. Model 1 has about 880,000 elements, whereas models 2 through 4 have approximately 700,000 elements. The beams were subjected to loads of 50, 100, 150, and 200 uN and deflections were measured at the bottom of the beam at the same distance from the clamp

where the load is applied. A Young's modulus of 219 GPa was used for the UO_2 matrix in all cases and results are shown in Table 4.7.

Table 4.7: Load-displacement data obtained in Abaqus™ for models with pore clusters moving from substrate to the middle and to the end of the beam.

Model No.	50 μN	100 μN	150 μN	200 μN	Slope	*E* (GPa)	%
1	1.89E-02	3.78E-02	5.68E-02	7.57E-02	2640	219	
2	1.99E-02	3.97E-02	5.96E-02	7.94E-02	2520	209	4.5%
3	1.95E-02	3.90E-02	5.85E-02	7.80E-02	2570	213	2.7%
4	1.94E-02	3.89E-02	5.83E-02	7.78E-02	2570	213	2.7%

The largest effect occurs when the pore cluster is close to the substrate, where a reduction of 4.6% on E is obtained with respect to the case with no pores. However, it is less than the 7% decrease predicted by equation (4) for the 2.5% pore fraction used. This is most likely due to the fact that the bottom row of pores in the cluster is very close to the neutral plane of the beam. The location of neutral plane is calculated to be 3.13 um away from the top of the beam using equation (3). Since pores close to the neutral plane do not contribute much to reducing the moment of inertia of the cross section, the effective porosity should be 1.67%. A 4.7% reduction is predicted using equation (4) for 1.67% pore fraction, which is very close to 4.6% reduction on E obtained from the simulations. This demonstrates that the effect of porosity is also sensitive to the pore position within the cross section.

When the pore cluster is moved along length towards the end of the beam, Young's modulus starts to increase, as stated above, since the stress and strains will decrease, leading to smaller increases in slopes. And also shorter arms for a smaller arc length, as well as smaller increase in deflections, as compared to those close to the clamp, even though the reduction in inertia is the same in all cases. Pores close to the clamp and large pores close to either the top or bottom surface of the micro-beams will have the largest effect and they can be present during actual experiments. The results suggest that creating FE models that account for the actual geometry and location of pores in the region close to the clamp, from perhaps one half of the length of the beam, should lead to more accurate estimations of the actual Young's modulus of the matrix, by matching the slope of the simulated load-deflection curves to those obtained experimentally by tuning the value E used in the simulations. Additional work is being carried out using anisotropic elasticity to estimate the sensitivity of the measurements to the orientation of the grains within the beams.

V CONCLUSIONS AND FUTURE WORK

5.1 Conclusions

The objective of this study was to create and develop simulation tools to study mechanical behavior of uranium dioxide at the sub-grain scale, with emphasis on measurement of elastic properties. This work was based on micro-scale mechanical testing, microstructure characterization and reconstruction, and finite element modeling to account for effects of material anisotropy, sample geometry, and porosity on the determination of mechanical properties from bending of micro-cantilever beams.

In detail, the following conclusions can be drawn from the experimental and simulation results:

1. 3-D finite element models were created based on the real geometry and dimension of the micro-cantilever beams used in the experiments. Size effect of substrate were studied using these models. The results indicate that the width of the substrate should be at least larger than that of the beam and it is enough if the width of the substrate can be twice that of the beam.

2. Effective Young's modulus was come up with to calculate Young's modulus of the beam that has bamboo structure. It is found that the value of effective Young's modulus obtained from bending is dominated by the behavior of about one half of the beam close to the substrate.

3. The model created using microstructure reconstruction was used to study the effect of pore location on the effective (apparent) Young's modulus measured from micro-cantilever experiments. These models were imported into Abaqus^{TM} for analysis. The results indicate that the presence of pore clusters close to the clamp, as well as large

pores close to the top or bottom surfaces of the beam can result in reductions in Young's modulus estimation from load-deflection curves measured in micro-cantilever beams where pore size and spacing are of the order of the beam dimensions.

4. The presence of pore clusters close to the substrate of the micro-cantilever beam, has the strongest effect on load-deflection behavior, leading to a reduction of stiffness that is the largest for any location of the pore cluster. It is also found that pore clusters located towards the middle of the span and close to the end of the beam only have a very small effect on the lad-deflection behavior.

5. When pores are close to the neutral plane, their effect becomes small. The location that pores have the biggest effect is at the top and bottom of the beam, which is away from neutral plane.

6. Better estimates of Young's modulus can be obtained from micro-cantilever experiments by accounting for porosity in about one half of the beam length close to the clamp.

7. The results provide insight into steps needed to estimate Young's modulus of porous material at sub-grain scale using micro-cantilever bending tests, especially when pore size and spacing are of the same magnitude as the beam and emphasize the importance of considering geometry and location of the pore in reducing stiffness of the beam.

5.2 Future Work:

1. One major focus in this work is sample processing. Heat-treating samples at 1460 °C for longer time might help to get larger grains to make it possible to manufacture

one or several micro-cantilever beams inside a single grain, which will facilitate studying single crystal behavior and allow macro-scale testing of multi-crystal samples.

2. Micro-cantilever beams with both larger length and larger length-height ratio need to be manufactured inside a single grain to facilitate the study of single crystal behavior under sub-grain level.

3. Microstructure reconstruction with much more layers needs to be performed, which will contribute to accurately depict the inner structure of the cantilever beam, thus allowing us to make much more accurate comparisons between simulation and experimental results.

4. The effect of pores will be further studied, taking their size, geometry and distribution into account, which will provide insight in studying porous material using micro-scale testing techniques.

5. High-temperature mechanical testing under micro-scale and macro-scale will be conducted in order to study mechanical behavior of UO_2 under environments closer to those found in nuclear reactors.

VI REFERENCES

[1] Goldberg, S., & Rosner, R. *Nuclear Reactors: Generation to Generation*. American Academy of Arts and Sciences. (2011).

[2] Deutch, J.: *Update of the MIT 2003 the future of nuclear power*. Cambridge, MA: MIT. (2009).

[3] World Nuclear Association, from <http://www.world-nuclear.org/info/nuclear-fuel-cycle/nuclear-wastes/radioactive-waste-management/>.

[4] World Nuclear Association. from <http://www.world-nuclear.org/info/nuclear-fuel-cycle/fuel-recycling/processing-of-used-nuclear-fuel/>.

[5] NDEP, "Locations map of spent nuclear fuel and High-Level radioactive waste." 2000. Web. < https://ndep.nv.gov/admin/wastemap.gif >.

[6] World Nuclear Association, from <http://www.world-nuclear.org/info/current-and-future-generation/nuclear-power-in-the-world-today/>.

[7] IEA, Electricity Information 2015, International Energy Agency, 2015.

[8] "IEA Atlas." 2015. Web. <http://energyatlas.iea.org/?subject=- 1118783123#>.

[9] "In Situ Leach (ISL) Mining of Uranium." 2015. from <http://www.world-nuclear.org/info/nuclear-fuel-cycle/mining-of-uranium/in-situ-leach-mining-of-uranium>.

[10] Nuclear Fuel Processes. from <http://www.nei.org/Knowledge-Center/Nuclear-Fuel-Processes>.

[11] Hanson, "Nuclear Fuel Assembly", Department of Energy.

[12] Wikipedia. Retrieved November 11, 2015, from <https://en.wikipedia.org/wiki/Nuclear_fission#cite_note-10>.

[13] Judd, A.: An introduction to the engineering of fast nuclear reactors. Cambridge University Press. (2014).

[14] Alam, T., Khan, M., Pathak, M., Ravi, K., Singh, R., & Gupta, S. A review on the clad failure studies. *Nuclear Engineering and Design*, 3658-3677. (2011).

[15] Zinkle, S., Terrani, K., Gehin, J., Ott, L., & Snead, L. Accident tolerant fuels for LWRs: A perspective. *Journal of Nuclear Materials*, 374-379. (2014).

[16] Olander, D.: Nuclear Fuels: Present and Future. Engineering Journal EJ, 1-28. (2009).

[17] Cacuci, D. *Handbook of nuclear engineering* (Vol. 1). New York: Springer. (2010).

[18] Shannon, B: Development of advanced accident tolerant fuels for commercial LWRs. *Nuclear News*, 83-91. (2014).

[19] Zirconium in the Nuclear Industry: Thirteenth International.

[20] Peralta, P.: Mechanical Behavior of UO_2 at Sub-grain Length Scales: Quantification of Elastic, Plastic and Creep Properties via Microscale Testing.

[21] Daniel, K., Andrew, M., Osman, A., Yongqiang, W., Stuart, M., & Peter, H.: Application of small-scale testing for investigation of ion-beam-irradiated materials. *Journal of Materials Research*, 27, pp 2724-2736 (2012).

[22] Anisotropy and Isotropy. Retrieved November 11, 2015, from <https://www.nde-ed.org/EducationResources/CommunityCollege/Materials/Structure/anisotro>.

[23] Nye, J.F., *Physical Properties of Crystals* (New York, NY: Oxford University,1985).

[24] Fritz, I.: Elastic properties of UO2 at high pressure. *Journal of Applied Physics*, 4353-4353.

[25] Lethbridge, Z., Walton, R., Marmier, A., Smith, C., & Evans, K.: Elastic anisotropy and extreme Poisson's ratios in single crystals. *Acta Materialia*, 6444-6451.

[26] Uchic, M., & Dimiduk, D.: A methodology to investigate size scale effects in crystalline plasticity using uniaxial compression testing. *Materials Science and Engineering: A*, 268-278.

[27] Armstrong, D., & Tarleton, E.: Bend Testing of Silicon Microcantilevers from 21°C to 770°C. *JOM*. (2015).

[28] Abad, M., Parker, S., Frazer, D., Figueiredo, M., Lupinacci, A., Kikuchi, K., & Hosemann, P.: Evaluation of the Mechanical Properties of Naturally Grown Multilayered Oxides Formed on HCM12A Using Small Scale Mechanical Testing. *Oxid Met Oxidation of Metals*, 211-231.(2015).

[29] Hosemann, P., Shin, C., & Kiener, D. (2015). Small scale mechanical testing of irradiated materials. *Journal of Materials Research*, 1231-1245. (2015).

[30] Armstrong, D., Wilkinson, A., & Roberts, S.: Measuring anisotropy in Young's modulus of copper using microcantilever testing. *Journal of Materials Research*, 3268-3276. (2009).

[31] Maio, D., & Roberts, S.: Measuring fracture toughness of coatings using focused-ion-beam-machined microbeams. *Journal of Materials Research*, 299-302. (2004).

[32] Stehle, H., Assmann, H., & Wunderlich, F.: Uranium dioxide properties for LWR fuel rods. *Nuclear Engineering and Design*, 230-260. (1974).

[33] Pensée, V., & He, Q.: Generalized self-consistent estimation of the apparent isotropic elastic moduli and minimum representative volume element size of heterogeneous media. International Journal of Solids and Structures, 2225-2243. (2006).

[34] Igata, N., & Domoto, K.: Fracture stress and elastic modulus of uranium dioxide including excess oxygen. *Journal of Nuclear Materials*, 317-322. (1972).

[35] Desai, T., Millett, P., Tonks, M., & Wolf, D.: Atomistic simulations of void migration under thermal gradient in UO2. *Acta Materialia*, 330-339. (2009).

[36] Vincent, P., Monerie, Y., & Suquet, P.: Porous materials with two populations of voids under internal pressure: II. Growth and coalescence of voids. *International Journal of Solids and Structures*, 507-526. (2009).

[37] Gatt, J., Monerie, Y., Laux, D., & Baron, D.: Elastic behavior of porous ceramics: Application to nuclear fuel materials. *Journal of Nuclear Materials*, 145-155. (2004).

[38] Wikipedia, from <https://en.wikipedia.org/wiki/Uranium>.

[39] Olander, D..: *Fundamental Aspects of Nuclear Reactor Fuel Elements*.(1976).

[40] Joung, C., Lee, S., Kim, S., Kim, H., & Sohn, D.: Fabrication method for UO2 pellets with large grains or a single grain by sintering in air. *Journal of Nuclear Materials*, 209-212. (2008).

[41] Higgs, J.D., Lewis, B.J., Thompson, W.T., and He, Z.: A conceptual model for the fuel oxidation of defective fuel. *Journal of Nuclear Materials.* 366 (2007) 99-128.

[42] Oliver, W., & Pharr, G.: An improved technique for determining hardness and elastic modulus using load and displacement sensing indentation experiments. *Journal of Materials Research*, 1564-1583. (1992).

[43] Oliver, W., & Pharr, G.: Measurement of hardness and elastic modulus by instrumented indentation: Advances in understanding and refinements to methodology. *Journal of Materials Research*, 3-20. (2003).

[44] Meshing your Geometry: When to Use the Various Element Types. (2013, November 4). from http://www.comsol.com/blogs/meshing-your-geometry-various-element-types/.